

# A transiting super-Earth in the radius valley and an outer planet candidate around HD 307842\*

XINYAN HUA<sup>1</sup>, SHARON XUESONG WANG<sup>1</sup>, JOHANNA K. TESKE<sup>2</sup>, TIANJUN GAN<sup>1</sup>, AVI SHPORER<sup>3</sup>,  
GEORGE ZHOU<sup>4</sup>, KEIVAN G. STASSUN<sup>5</sup>, MARKUS RABUS<sup>6</sup>, STEVE B. HOWELL<sup>7</sup>, CARL ZIEGLER<sup>8</sup>,  
JACK J. LISSAUER<sup>9</sup>, JOSHUA N. WINN<sup>10</sup>, JON M. JENKINS<sup>11</sup>, ERIC B. TING<sup>12</sup>, KAREN A. COLLINS<sup>11</sup>,  
ANDREW W. MANN<sup>12</sup>, WEI ZHU<sup>1</sup>, SU WANG<sup>13</sup>, R. PAUL BUTLER<sup>14</sup>, JEFFREY D. CRANE<sup>14</sup>,  
STEPHEN A. SHECTMAN<sup>14</sup>, LUKE G. BOUMA<sup>15</sup>, CÉSAR BRICEÑO<sup>16</sup>, DIANA DRAGOMIR<sup>17</sup>, WILLIAM FONG<sup>3</sup>,  
NICHOLAS LAW<sup>12</sup>, JENNIFER V. MEDINA<sup>18</sup>, SAMUEL N. QUINN<sup>11</sup>, GEORGE R. RICKER<sup>3</sup>, RICHARD P. SCHWARZ<sup>11</sup>,  
SARA SEAGER<sup>19, 3, 20</sup>, RAMOTHOLO SEFAKO<sup>21</sup>, CHRIS STOCKDALE<sup>22</sup>, ROLAND VANDERSPEK<sup>3</sup>, AND JOEL VILLASEÑOR<sup>3</sup>

<sup>1</sup>Department of Astronomy, Tsinghua University, Beijing 100084, China

<sup>2</sup>Earth and Planets Laboratory, Carnegie Institution for Science, 5241 Broad Branch Road, NW, Washington, DC 20015, USA

<sup>3</sup>Department of Physics and Kavli Institute for Astrophysics and Space Research, Massachusetts Institute of Technology, Cambridge, MA 02139, USA

<sup>4</sup>Centre for Astrophysics, University of Southern Queensland, Queensland, Australia

<sup>5</sup>Department of Physics and Astronomy, Vanderbilt University, Nashville, TN 37235, USA

<sup>6</sup>Departamento de Matemática y Física Aplicadas, Facultad de Ingeniería, Universidad Católica de la Santísima Concepción, Alonso de Rivera 2850, Concepción, Chile

<sup>7</sup>NASA Ames Research Center, Moffett Field, CA 94035, USA

<sup>8</sup>Department of Physics, Engineering and Astronomy, Stephen F. Austin State University, 1936 North St, Nacogdoches, TX 75962, USA

<sup>9</sup>Space Science & Astrobiology Division, MS 245-3, NASA Ames Research Center, Moffett Field, CA 94035, USA

<sup>10</sup>Department of Astrophysical Sciences, Princeton University, 4 Ivy Lane, Princeton, NJ 08544, USA

<sup>11</sup>Center for Astrophysics | Harvard & Smithsonian, 60 Garden Street, Cambridge, MA 02138, USA

<sup>12</sup>Department of Physics and Astronomy, The University of North Carolina at Chapel Hill, Chapel Hill, NC 27599-3255, USA

<sup>13</sup>Purple Mountain Observatory, No.10 Yuanhua Road, Nanjing, 210023, China

<sup>14</sup>Observatories of the Carnegie Institution for Science, 813 Santa Barbara Street, Pasadena, CA 91101, USA

<sup>15</sup>Cahill Center for Astrophysics, California Institute of Technology, Pasadena, CA 91125, USA

<sup>16</sup>Cerro Tololo Inter-American Observatory, Casilla 603, La Serena, Chile

<sup>17</sup>Department of Physics and Astronomy, University of New Mexico, 210 Yale Blvd NE, Albuquerque, NM 87106, USA

<sup>18</sup>Space Telescope Science Institute, 3700 San Martin Drive, Baltimore, MD, 21218, USA

<sup>19</sup>Department of Earth, Atmospheric, and Planetary Sciences, Massachusetts Institute of Technology, Cambridge, MA 02139, USA

<sup>20</sup>Department of Aeronautics and Astronautics, Massachusetts Institute of Technology, Cambridge, MA 02139, USA

<sup>21</sup>South African Astronomical Observatory,

P.O. Box 9, Observatory, Cape Town 7935, South Africa

<sup>22</sup>Hazelwood Observatory, Australia

## ABSTRACT

We report the confirmation of a *TESS*-discovered transiting super-Earth planet orbiting a mid-G star, HD 307842 (TOI-784). The planet has a period of 2.8 days, and the radial velocity (RV) measurements constrain the mass to be  $9.67^{+0.83}_{-0.82} M_{\oplus}$ . We also report the discovery of an additional planet candidate on an outer orbit that is most likely non-transiting. The possible periods of the planet candidate are approximately 20 to 63 days, with the corresponding RV semi-amplitudes expected to range from 3.2 to 5.4 m/s and minimum masses from 12.6 to 31.1  $M_{\oplus}$ . The radius of the transiting planet (planet b) is  $1.93^{+0.11}_{-0.09} R_{\oplus}$ , which results in a mean density of  $7.4^{+1.4}_{-1.2} \text{ g/cm}^3$  suggesting that TOI-784b is likely to be a rocky planet though it has a comparable radius to a sub-Neptune. We found TOI-784b is located at the lower edge of the so-called “radius valley” in the radius vs. insolation plane, which is consistent with the photoevaporation or core-powered mass loss prediction. The *TESS*

Corresponding author: Xinyan Hua, Sharon Xuesong Wang  
huaxinyan1996@gmail.com, sharonw@tsinghua.edu.cn

\* This paper includes data gathered with the 6.5 meter Magellan Telescopes located at Las Campanas Observatory, Chile.

data did not reveal any significant transit signal of the planet candidate, and our analysis shows that the orbital inclinations of planet b and the planet candidate are  $88.60^{+0.84}_{-0.86}$  and  $\leq 88.3^\circ - 89.2^\circ$ , respectively. More RV observations are needed to determine the period and mass of the second object, and search for additional planets in this system.

*Keywords:* Exoplanet astronomy; Transit photometry; Radial velocity

## 1. INTRODUCTION

Planets in extrasolar systems are common in the universe. In the past few decades, over 5000 exoplanets were discovered and confirmed. NASA’s *Kepler* space telescope discovered thousands of transiting planet candidates with most of them having a size between Earth and Neptune (Borucki et al. 2010). Fulton et al. (2017) studied the size distribution of 2025 *Kepler* planets (the California-*Kepler* Survey sample) in fine detail and found a bimodal structure with a gap near  $1.5 - 2.0 R_\oplus$  separating super-Earths and sub-Neptunes, which is referred as the “radius valley”. Weiss et al. (2018) further claimed that this valley also exists in multi-planet systems.

The formation process of the radius valley and its position as a function of other planetary or host stars’ parameters are still under debate. A positive relationship between the transition radius and planet insolation flux was derived from the CKS sample (Martinez et al. 2019; Petigura et al. 2022), which can be explained by the photoevaporation scenario (e.g. Owen & Wu 2017; Lopez & Rice 2018; Fulton & Petigura 2018), where the close-in planets become stripped cores while the outer ones can keep their gas envelopes and thus have larger sizes. On the other hand, Cloutier & Menou (2020) estimated an opposite correlation using 275 *Kepler* and 53 *K2* planets around M and K type stars, which is consistent with a gas-poor formation theory (e.g., Lopez & Rice 2018), where most rocky planets are formed after the discs dissipate and thus without initial gaseous envelopes.

Radial velocity (RV) follow-up observations on planets with sizes near the radius valley could shine more light on the structure and origin of the valley, especially for the “keystone” planets where different models predict different fractions of volatile (e.g., Cloutier & Menou 2020; Cloutier et al. 2020). The mass measurements from RVs would provide some constraints on the bulk composition of transiting planets, thus revealing how planetary composition might shift across the radius valley (e.g., Luque & Pallé 2022). Obtaining precise mass measurements of super-Earths and sub-Neptunes is also important for reliably characterizing the composition of their atmosphere (if any; Batalha et al. 2019).

In addition to the mass and bulk density measurement, RV follow-up can also reveal additional planets in the system, either non-transiting or yet to be detected by transits, which is more important for mapping out the system architecture for transiting planets discovered by the *Transiting Exoplanet Survey Satellite* (*TESS*; Ricker et al. 2015) given its relatively shorter baseline compared with *Kepler*. Studies on planet multiplicity found that multi-planet systems are common (e.g., 40% among systems with super-Earths or sub-Neptunes discovered by *Kepler*; Batalha et al. 2013), so RV follow-up observations on transiting planets often turn out to be fruitful (e.g., Lacedelli et al. 2021; Lubin et al. 2022). Revealing the non-transiting planets in systems with single transiting planets can be of particular interest, as it directly addresses the previously identified “*Kepler* dichotomy”, where a surplus of *Kepler* single-transiting systems was inconsistent with predictions from earlier population synthesis models with relatively low mutual inclinations, but consistent with an additional population of multi-planet systems with large mutual inclinations (e.g., Lissauer et al. 2011; Hansen & Murray 2013; Ballard & Johnson 2016). This “dichotomy” appears to hold for both M dwarfs and Sun-like stars, and it can not be fully explained by selection biases (e.g. Zink et al. 2019). Different scenarios were proposed to explain the *Kepler* dichotomy (e.g. Mulders et al. 2018; Zhu et al. 2018; He et al. 2019; He et al. 2020), but the intrinsic mutual inclination distribution for multi-planet systems still remains uncertain. More samples of well-charactered multi-planet systems, either with RVs or TTVs, are needed for investigations on the intrinsic mutual inclination distribution of planets and studies on system architectures in general (e.g., see review by Weiss et al. 2022).

In this work, we report a *TESS* discovered transiting super-Earth, TOI-784b, and an additional Neptune-mass planet candidate in the system using RV follow-up data taken by the Magellan *TESS* Survey (MTS; Teske et al. 2021). We organize this paper as follows: we first describe our observational data and data reduction processes in Section 2, as well as results from direct imaging. We then introduce the stellar characterization in Section 3. Section 4 presents the detailed photometry

and radial velocity modeling to constrain the planetary properties. We discuss our results and present our conclusions in Section 5.

## 2. OBSERVATIONS

### 2.1. Photometry

#### 2.1.1. TESS

The *TESS* mission is an all-sky survey to discover transiting exoplanets (Ricker et al. 2015), with a field of view of  $24^\circ \times 96^\circ$ , observing in Sectors each lasting about 27 days. From July 2018 to July 2020, *TESS* mapped almost the whole sky in its two-year Primary Mission and then re-observed the southern ecliptic hemisphere during Year 3 (July 2020–July 2021) for its first Extended Mission. *TESS* recently completed its first extended mission slightly over four years from the start of science observations in July 2018 and has now commenced its second extended mission.

HD 307842 (TIC 460984940, hereafter TOI-784) was observed by the *TESS* mission and announced as TOI-784 after its Cycle 1 observation in Sectors 10 (March 26 to April 22, 2019) and 11 (April 22 to May 21, 2019) with a two-minute cadence using camera 3. In Cycle 3, TOI-784 was revisited with the same mode in Sector 37 (April 2 to April 28, 2021) and 38 (April 28 to May 26, 2021). The raw photometric data were first reduced by the Science Processing Operations Center (SPOC; Jenkins et al. 2016) pipeline at NASA Ames Research Center, which extracted the light curve using Simple Aperture Photometry (SAP) and further calibrated for instrument systematics using the Presearch Data Conditioning (PDC) algorithm.

The SPOC Transiting Planet Search (TPS; Jenkins 2002; Jenkins et al. 2010; Jenkins et al. 2020) of the light curve via an adaptive, noise-compensating matched filter revealed a transit signal with a 2.8-day period on 23 May 2019. An initial limb-darkened transit model was fitted (Li et al. 2019) and a suite of diagnostic tests were conducted to help make or break the planetary nature of the signal(s) (Twicken et al. 2018), presented in the Data Validation reports available on the Mikulski Archive for Space Telescopes<sup>1</sup> (MAST). In this case the transit signal failed the ghost diagnostic test, but visual inspection of the difference images indicates that the transit source is located on the target. The *TESS* Science Office reviewed the vetting reports and issued an alert for TOI-784b on 5 June 2019 (Guerrero et al. 2021).

<sup>1</sup> <https://archive.stsci.edu>

The Presearch Data Conditioning Simple Aperture Photometry light curve file (PDCSAP flux; Stumpe et al. 2012; Smith et al. 2012; Stumpe et al. 2014) for photometry analyses in this work (see Section 4.1) was downloaded from MAST using the `lightkurve` package (Lightkurve Collaboration et al. 2018).

#### 2.1.2. Las Cumbres Observatory: Sinistro

We collected three sets of ground-based light curves for TOI-784 using the Las Cumbres Observatory Global Telescope (LCOGT<sup>2</sup>) network (Brown et al. 2013) on 26<sup>th</sup> Feb. 2020, 13<sup>rd</sup> Mar. 2020 and 21<sup>st</sup> Jan. 2021 to refine the transit ephemeris and rule out the nearby eclipsing binary scenario. We used the *TESS* Transit Finder, which is a customized version of the *Tapir* software package (Jensen 2013), to schedule the transit observation. All three observations were taken with the Sinistro cameras in the Pan-STARRS *z*-short band ( $z_s$ ) with exposure times of 70, 70, and 30 s. We carried out a photometric analysis and extracted the light curves using *AstroImageJ* (Collins et al. 2017). We excluded all nearby stars within 2.5' as the source that may cause the *TESS* signal with brightness difference down to  $\Delta T \sim 9.5$  mag and tentatively detected the signal on target. The data are publicly available on ExoFOP<sup>3</sup>.

#### 2.1.3. Other Archival Ground-based Photometry

We found 963 *V*-band archival measurements of TOI-784 from the ASAS database<sup>4</sup> spanning from November 21, 2000, to December 3, 2009.<sup>5</sup> Following the ASAS documentation, we selected 883 data points ranked as grades A and B, which represent the highest-quality measurements. We applied a 3-sigma clipping rejection, after which 35 measurements were masked and 848 were left. Considering the *V* magnitude of our target ( $\sim 9.4$ ) and the observing aperture scale, the data points marked as “MAG\_3” were used in our analysis as recommended by ASAS<sup>6</sup>. We calculated the Generalized Lomb-Scargle (GLS) Periodogram using the python module `PyAstronomy.pyTiming.pyPeriod.Gls()` to search for

<sup>2</sup> <https://lco.global/>

<sup>3</sup> <https://exofop.ipac.caltech.edu/tess/target.php?id=88902249>

<sup>4</sup> <http://www.astrouw.edu.pl/asas/?page=aasc&catsrc=asas3>

<sup>5</sup> We also found archival photometry data from ASAS-SN (<https://asas-sn.osu.edu/photometry>), in which we saw a long term trend spanning in the time baseline ( $\sim 904$  days), so we did not adopt it. We found no archival data from WASP (<https://wasp.cerit-sc.cz/form>).

<sup>6</sup> Indices from 0–4 indicate 5 apertures of 2–6 pixels wide. Small ones are better for faint stars while large ones for bright stars, roughly following the relation of  $aperture\ index = 12 - V$ . See <http://www.astrouw.edu.pl/asas/explanations.html> for more detailed explanations.

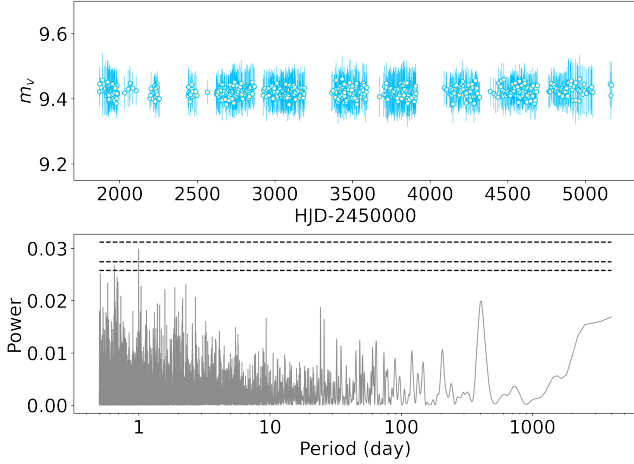


**Figure 1.** The ASAS V-band photometry (top) and its GLS periodogram. The three dashed lines from top to bottom in the lower panel correspond to 1%, 5%, and 10% significance threshold levels, respectively. The maximum signal appears at around 1 day, which is likely an alias due to the observing cadence. No significant signal was identified for the stellar rotation.

the rotation signal of the host star<sup>7</sup>. Results are shown in Figure 1; the three black dashed lines from top to bottom in the figure correspond to false-alarm probabilities (FAP) of 1%, 5%, and 10%, which means that there is a 1%, 5%, or 10% chance, respectively, that the observed signal is a false positive. The FAP values were computed via the default function within the `GLS()` module with the default normalization assumption described in Zechmeister & Kürster (2009). We found no significant rotation modulation, suggesting that TOI-784 is probably an old, slowly rotating and photometrically quiet star. The peak around one day is likely an alias resulting from the observation cadence.

## 2.2. Spectroscopy

### 2.2.1. PFS

We collected a total of 35 RV data points using the Planet Finder Spectrograph (PFS; Crane et al. 2006, 2008, 2010) on the 6.5-meter Magellan II Clay telescope at Las Campanas Observatory in Chile. PFS is a high-resolution, optical echelle spectrograph that covers a wavelength band of 391–734 nm with a resolving power of  $R \sim 130,000$  using the  $0.3'' \times 2.5''$  slit. The RV precision of PFS on nearby, bright, and photospherically quiet stars is typically 0.5–1.0 m/s. The spectral data reduction and RV extraction were performed using a customized pipeline (Butler et al. 1996).

<sup>7</sup> A same analysis was applied using the *TESS* light curve, which alerted no evident signal as expected.

Our PFS data were obtained as part of the Magellan *TESS* Survey (MTS; Teske et al. 2021), a project designed to study a sample of 30 well-characterized small planets with radii  $< 3R_{\oplus}$  to reveal their population statistics such as the M-R relation (Wolfgang et al. 2016; Weiss et al. 2018), the “radius gap” around  $1.8R_{\oplus}$  (Fulton et al. 2017; Petigura et al. 2022), and other stellar properties/system architecture in order to reveal their formation and evolution processes. A sample of 30 targets were selected using a quantified merit function among the *TESS* Objects of Interest (TOIs) from the Year 1 observations of *TESS* (therefore only includes the southern hemisphere), and TOI-784 was among the initial sample of 30 at the beginning of MTS but later on dropped off the list due to the refinement of stellar and planetary parameters of TOIs over time.

MTS adopts a specific observing strategy to minimize selection bias (see Teske et al. 2021 for more details about the observing cadence design). TOI-784 received a High Cadence grade for its coverage, with 22 RV observations taken from UT March 6 to UT March 17 in 2020 and 9 RV data points between UT May 22 and UT May 29 in 2021, and MTS stopped observing TOI-784 afterward as it dropped out of the target list. We then collected four more data points from UT 2022-3-14 to 2022-3-25 in order to characterize the additional long-period planet candidate, as the RV fitting results using the first year’s data showed a linear trend in the residuals (see Section 4.2 for more). With a typical exposure time of 10 to 20 minutes depending on the seeing, the reported internal RV precision  $\sigma_{RV}$  of PFS on TOI-784 is 0.7–1.0 m/s. See Table 1 for all the PFS RVs used in this work.

**Table 1.** RV measurements

Time	RV (m/s)	Uncertainty (m/s)	Instrument
2458914.68102	-6.02	0.83	PFS
2458914.80040	-8.24	0.87	PFS
2458915.68459	-3.32	0.79	PFS
2458915.75693	-3.82	0.78	PFS
2458916.71986	0.34	0.77	PFS
2458917.65647	-6.89	0.74	PFS
2458917.73457	-5.19	0.74	PFS
2458918.67521	0.27	0.91	PFS
2458918.75249	2.39	0.72	PFS
2458919.66161	0.12	0.68	PFS
2458919.74236	3.05	0.70	PFS

(To be continued)

Time	RV (m/s)	Uncertainty (m/s)	Instrument
2458920.65817	-5.21	0.64	PFS
2458920.71749	-4.78	0.64	PFS
2458921.67109	3.56	0.65	PFS
2458921.73069	6.03	0.62	PFS
2458923.63457	-0.01	0.71	PFS
2458923.70633	-1.72	0.75	PFS
2458924.62670	6.63	0.61	PFS
2458924.70608	6.77	0.70	PFS
2458924.77554	8.45	0.72	PFS
2458925.62948	1.55	0.67	PFS
2458925.71178	-0.09	0.72	PFS
2459356.50045	-6.68	0.99	PFS
2459356.57079	-6.90	1.06	PFS
2459358.57198	0.90	1.09	PFS
2459359.49081	-6.39	1.11	PFS
2459359.58574	-8.32	1.03	PFS
2459361.45964	0.80	1.03	PFS
2459361.58363	0.59	1.14	PFS
2459363.46677	3.25	1.08	PFS
2459363.55417	5.02	1.04	PFS
2459652.72417	-0.57	0.73	PFS
2459654.70344	2.93	0.70	PFS
2459657.67591	0.00	0.71	PFS
2459663.67738	-1.96	1.00	PFS
2459336.22205515	15163.8	10.5	NRES1
2459344.41512404	15157.3	9.1	NRES1
2459346.23537912	15136.2	9.2	NRES1
2459348.25530748	15198.2	9.0	NRES1
2459353.21427107	15118.7	9.4	NRES1
2459357.35987432	15162.1	11.0	NRES1
2459360.33375668	15153.9	9.8	NRES1
2459369.30694576	15142.5	8.7	NRES1
2459376.32741634	15122.2	8.9	NRES1
2459377.24338348	15102.5	8.9	NRES1
2459411.24579787	15080.6	8.1	NRES1
2459578.74273868	14871.4	5.7	NRES2
2459580.74290906	14877.7	5.5	NRES2
2459584.74664902	14918.7	5.3	NRES2
2459593.79187993	14922.3	9.0	NRES2
2459597.72988968	14834.6	7.9	NRES2
2459601.75295545	14930.1	8.5	NRES2
2459602.75137792	14925.8	6.8	NRES2
2459604.79780727	14882.6	6.4	NRES2
2459609.68250136	14854.9	4.9	NRES2
2458909.692940	15780.0	27.0	CHIRON
2458916.735210	15743.0	24.0	CHIRON
2459428.457080	15786.0	20.0	CHIRON

### 2.2.2. NRES

We acquired TOI-784 spectra using the Las Cumbres Observatory’s (LCO) Network of Robotic Echelle Spectrographs (NRES; [Siverd et al. 2018](#)). LCO-NRES consists of four high-resolution optical echelle spectrographs (located in Chile, South Africa, Israel, and USA) with a resolution of  $R \sim 53,000$  and a wavelength range spanning 380–860 nm. Each spectrograph is fed by two fibers: one fiber is illuminated by the stellar light coming from a 1-meter telescope at the respective site, and the second one is fed by a ThAr reference lamp. At the beginning of each night, each NRES unit automatically takes calibration images including bias, dark, flat, and ThAr frames.

We randomly scheduled our observations with a time span of 1–4 days to avoid any observing bias ([Burt et al. 2018](#)) and constrained the lunar separation threshold to  $30^\circ$  and the airmass to  $< 1.6$ . Our exposure times ranged from 30 to 40 min, reaching an SNR between 40 and 90 at 5130 Å. We collected 12 spectra in total from May to July 2021 on the NRES unit in South Africa (CPT) and 18 spectra from December 2021 to January 2022 on the unit in Chile (LSC). After binning multiple shots taken on the same nights to enhance the signal-to-noise ratio (SNR), we ended up with 20 RV data points from LCO-NRES. The raw spectra were calibrated and wavelength corrected using the CERES pipeline ([Brahm et al. 2017](#)). By cross-correlating the observed spectra with a binary mask, the CERES pipeline also delivers radial velocity measurements for each spectrum. The reported internal RV precision on TOI-784 is typically around 10 m/s. See Table 1 for all the NRES RVs.

### 2.2.3. CHIRON

We obtained three observations of TOI-784 via the CHIRON facility between March 2020 and August 2021 to provide reconnaissance spectroscopic vetting of the target. CHIRON is a fiber-fed high-resolution echelle spectrograph at the SMARTS 1.5-m telescope located at Cerro Tololo Inter-American Observatory, Chile ([Tokovinin et al. 2013](#)) with a spectral coverage of 410 to 870 nm. TOI-784 was observed in the *fiber* mode, with a spectral resolving power of  $R \sim 28,000$  and an exposure time of 5 minutes. The RV precision is about 20–30 m/s. The spectra were extracted through the official CHIRON pipeline described in [Paredes et al. \(2021\)](#). We derived RVs from a least-squares deconvolution between the observation and a non-rotating synthetic template, which is generated via the ATLAS9 atmosphere models ([Castelli & Kurucz 2003](#)) at the given spectral parameters of the targets. The derived broadening profile is fitted with a kernel accounting for the effects of ro-

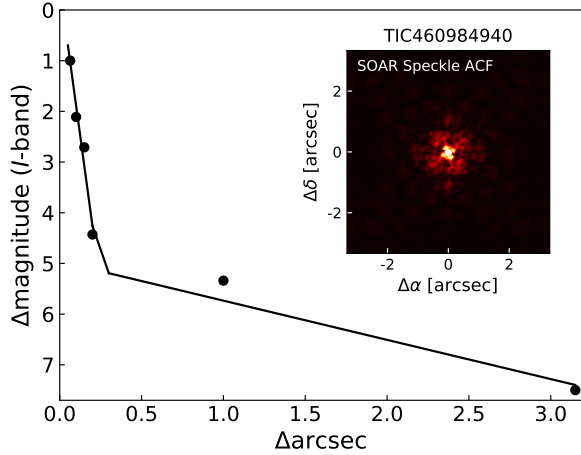


**Figure 2.** SOAR high-resolution speckle image contrast limits in the Cousins-I band-pass. The inserts show the speckle auto-correlation function. SOAR did not detect a nearby companion to TOI-784.

tational, macroturbulent, instrumental broadening, and radial velocity shift. The CHIRON spectra were also used to estimate stellar parameters, which is described in detail in Section 3.2. The CHIRON RVs are listed in Table 1.

### 2.3. High-Resolution Speckle Imaging

Spatially close stellar companions can create false-positive transit signals and/or lessen the transit depth, causing the exoplanet’s radius to be underestimated. Thus, determination of the “third-light” flux contamination from the close companion stars is important to properly account for or rule out. To search for close-in bound (or line of sight) companions unresolved in *TESS* or other ground-based follow-up observations, we obtained high-resolution imaging speckle observations of TOI-784.

#### 2.3.1. SOAR HRcam

We searched for stellar companions to TOI-784 with speckle imaging on the 4.1-m Southern Astrophysical Research (SOAR) telescope (Tokovinin 2018) on 14 July 2019 UT, observing in Cousins I-band, a similar visible bandpass as *TESS*. This observation was sensitive to a 5.4-magnitude fainter star at an angular distance of 1 arcsec from the target. More details of the observations within the SOAR *TESS* survey are available in Ziegler et al. (2020). The  $5\sigma$  detection sensitivity and speckle auto-correlation functions from the observations are shown in Figure 2. No nearby stars were detected within  $3''$  of TOI-784 in the SOAR observations.

#### 2.3.2. Gemini Zorro

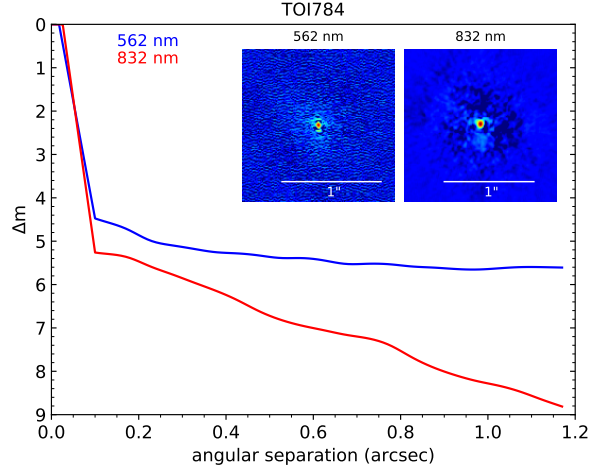


**Figure 3.** Zorro high-resolution speckle image contrast limits in both 562 and 832 nm band-passes. The inserts show the reconstructed images in both band-passes and that TOI-784 is a single star to the contrast levels achieved (1.3 to 77.5 AU).

TOI-784 was observed on 2020 March 12 UT using the Zorro speckle instrument on the Gemini South 8-m telescope<sup>8</sup>. Zorro provides simultaneous speckle imaging in two bands (562 nm and 832 nm) with output data products including a reconstructed image with robust contrast limits on companion detections. Three sets of  $1000 \times 0.06$  sec exposures were collected and subjected to Fourier analysis in our standard reduction pipeline (see Howell et al. 2011). Figure 3 shows our final contrast curves and our reconstructed speckle images. We find that TOI-784 is a single star with no companion brighter than 5–9 magnitudes below that of the target star from the diffraction limit (20 mas) out to  $1.2''$ . At the distance of TOI-784 ( $d = 64.6$  pc) these angular limits correspond to spatial limits of 1.3 to 77.5 AU.

## 3. STELLAR CHARACTERISATION

### 3.1. Spectral Energy Distribution

As an independent check on the fundamental parameters of the host star, we carry out an analysis of the broadband Spectral Energy Distribution (SED) together with the *Gaia* EDR3 parallax in order to determine an independent, empirical measurement of the stellar radius, following the procedures described in Stassun & Torres (2016), Stassun et al. (2017), and Stassun & Torres (2018). We pull the  $BV$  magnitudes from Mermilliod (2006), the  $B_T V_T$  magnitudes from *Tycho-2*, the  $JHK_S$  magnitudes from *2MASS*, the W1–W4 magnitudes from *WISE*, and the three *Gaia* magnitudes  $G, G_{BP}, G_{RP}$ .

<sup>8</sup> <https://www.gemini.edu/sciops/instruments/alopeke-zorro/>

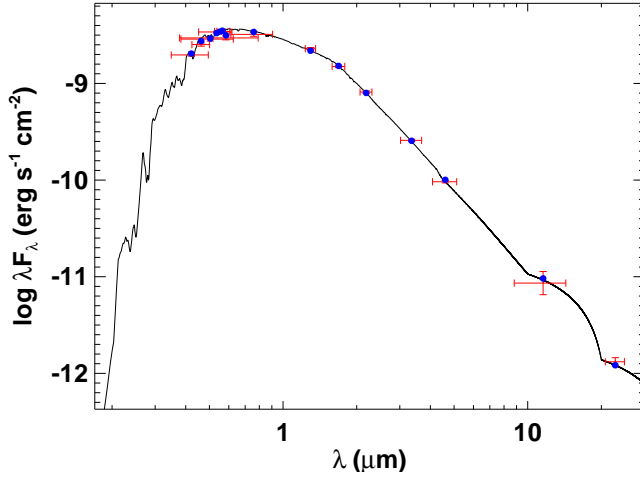


**Figure 4.** The best SED fit for TOI-784. Red symbols represent the observed photometric measurements, where the horizontal bars represent the effective width of the bandpass. Blue symbols are the model fluxes from the best-fit Kurucz atmosphere model (black solid line, Kurucz 1979; Castelli & Kurucz 2003).

Together, the available photometry spans the full stellar SED over the wavelength range  $0.4\text{--}22\text{ }\mu\text{m}$  (see Figure 4).

We perform a fit using Kurucz stellar atmosphere models, with the  $T_{\text{eff}}$ ,  $\log g$ , and  $[\text{Fe}/\text{H}]$  taken from the spectroscopic analysis (see below). The remaining parameter is the extinction ( $A_V$ ), which we constrained to be no larger than the full line-of-sight extinction from the dust maps of Schlegel et al. (1998). The resulting fit is shown in Figure 4 with a reduced  $\chi^2$  of 1.2 and best-fit extinction of  $A_V = 0.15 \pm 0.03$ . Integrating the model SED gives the bolometric flux at Earth of  $F_{\text{bol}} = 5.423 \pm 0.063 \times 10^{-9} \text{ erg s}^{-1} \text{ cm}^{-2}$ . Taking the  $F_{\text{bol}}$  and  $T_{\text{eff}}$  together with the *Gaia* parallax, with no adjustment for systematic parallax offset (see, e.g., Stassun & Torres 2021), gives the stellar radius as  $R_\star = 0.907 \pm 0.017 R_\odot$ . We can also estimate the stellar mass empirically via  $R_\star$  together with the spectroscopic  $\log g$ , which gives  $M_\star = 0.91 \pm 0.10 M_\odot$ , and which is consistent with the value of  $0.95 \pm 0.06 M_\odot$  inferred from the empirical relations of Torres et al. (2010).

Finally, using  $R_\star$  together with the spectroscopically-estimated rotational velocity ( $v \sin i$ ; see below), we can infer the stellar rotation period, which gives  $P_{\text{rot}}/\sin i = 41.7 \pm 11.4 \text{ d}$ . That rotation period yields an estimated system age via empirical gyrochronology relations (Mamajek & Hillenbrand 2008) of  $7.8 \pm 3.4 \text{ Gyr}$ . We caution the readers that the rotation period and age estimates are both based on the poorly constrained  $v \sin i$  value from spectroscopy, and thus they serve as only a rough

check to confirm that TOI-784 is an old star. We summarize the basic information of HD 307842 in Table 2.

### 3.2. Spectroscopic Parameters

To estimate the stellar parameters of TOI-784, we followed Zhou et al. (2020) and compared the CHIRON spectra against that of a library of  $\sim 10,000$  observed spectra previously classified via the Spectroscopic Classification Pipeline (SPC; Buchhave et al. 2012). The library is interpolated via a gradient-boosting regressor implemented in the `scikit-learn` package. We found a best fit effective temperature of  $5558 \pm 100 \text{ K}$ , surface gravity of  $\log g_\star = 4.48 \pm 0.10$ , and metallicity of  $[\text{Fe}/\text{H}] = -0.13 \pm 0.08$  for TOI-784. The standard deviation from the stellar parameters derived from each spectrum are very small (31 K, 0.03 dex, and 0.03 dex, respectively), showing that the photon-limited uncertainties for the stellar parameters are significantly smaller than associated model-dependent uncertainties. Considering that the stellar properties are relatively Sun-like where models are well-calibrated, we quoted a minimum temperature error of 100 K, which is the floor systematic uncertainty ( $\sim 2\%$  in temperature) recommended in Tayar et al. (2022).

In addition to the spectroscopic atmospheric parameters, we also measured the star’s projected rotational broadening velocity  $v \sin i$  through a least-squares deconvolution analysis. As per Section 2.2.3, the line broadening profile is modeled via a convolution of kernels describing the rotational, macroturbulent, and instrumental broadening effects. We found that we cannot resolve the rotational broadening of the star at the given instrumental resolution, measuring a maximum broadening of  $< 3 \text{ km s}^{-1}$  from the CHIRON observations. Nevertheless, we can safely conclude that the star is rotating at a rather slow speed, as we have mentioned in the GLS periodogram test of ground-based photometry that indicates a very weak rotation signal as well (see Section 2.1.3).

Following the procedure in Lehtinen et al. (2016) (Equations (6)-(9)), we estimated the logarithmic  $R'_{HK}$  of TOI-784 based on the PFS spectra. There are 13 among 35 PFS spectra having valid S-index measurements and are therefore used to calibrate the final  $\log R'_{HK}$ . An average value of  $-4.99$  was obtained after the calculations. We then converted it to the age ( $\log \tau$ ) of the target using Equation (3) in Mamajek & Hillenbrand (2008) and find that  $\log \tau \sim 9.8$ . Thus it is not surprising that TOI-784 has a low measured  $v \sin i$ , given that  $\log R'_{HK}$  falls into the “inactive” range of  $-5.10$  to  $-4.75$  as classified by Henry et al. (1996). The S-index has a median value of  $\sim 0.180$ , and it exhibits little

**Table 2.** Basic information of HD 307842

Parameter	Value	Description
TIC ID <sup>1</sup>	460984940	<i>TESS</i> Input Catalog
TOI ID <sup>1</sup>	784	<i>TESS</i> Objects of Interest
R.A. (J2000) <sup>2</sup>	10 <sup>h</sup> 37 <sup>m</sup> 21.88 <sup>s</sup>	Right Ascension
Dec. (J2000) <sup>2</sup>	−63°39′18.09″	Declination
$\mu_\alpha$ (mas/yr) <sup>2</sup>	3.413 ± 0.012	Proper Motion
$\mu_\delta$ (mas/yr) <sup>2</sup>	−154.788 ± 0.011	Proper Motion
$\varpi$ (mas) <sup>2</sup>	15.4833 ± 0.0108	Parallax distance
$D$ (pc) <sup>2</sup>	64.59 ± 0.05	Stellar distance
RV (km/s) <sup>3</sup>	15.06 ± 0.66	Radial velocity
$T_{\text{eff}}$ (K) <sup>4</sup>	5558 ± 100	Effective temperature
$\log g_\star$ (dex) <sup>4</sup>	4.48 ± 0.10	Surface gravity
[Fe/H] (dex) <sup>4</sup>	−0.13 ± 0.08	Stellar metallicity
$v \sin i$ (km/s) <sup>4</sup>	≲ 1.1 ± 0.3	Rotation speed
$T^1$	8.705 ± 0.017	T band magnitude
$V^1$	9.412 ± 0.003	V band magnitude
$\log R'_{HK}$ <sup>4</sup>	−4.99	
$R_\star$ (R <sub>⊙</sub> ) <sup>4</sup>	0.907 ± 0.017	Stellar radius
$M_\star$ (M <sub>⊙</sub> ) <sup>4</sup>	0.91 ± 0.10	Stellar mass

NOTE—1. Guerrero et al. (2021); 2. Gaia Collaboration (2020); 3. Gaia Collaboration (2018); 4. This work.

variation with a standard deviation of  $\sim 0.005$ , further indicating that TOI-784 is an inactive star.

TOI-784 is likely to have no wide-orbiting stellar companions since we found no matches in the catalogs from Brandt (2021) or Behmard et al. (2022), which provided cross-calibrations of Hipparcos or TOIs with Gaia EDR3 to search for stellar companions.

#### 4. ESTIMATES OF PLANETARY PARAMETERS

##### 4.1. Photometry analysis

###### 4.1.1. Transit Fit

We refer to the planet candidate and its parameters with an index of “c” for convenience in the following analyses, though it is not confirmed to be a planet as our RV data do not fully cover one orbital phase.

We used the *Juliet* package (Espinoza et al. 2019) to model the *TESS* PDCSAP flux after removing all NaN values and outliers. *Juliet* generates the transit model via *batman* (Kreidberg 2015) and supports Nested Samplers either using the MultiNest algorithm (Feroz & Hobson 2008; Feroz et al. 2009; Feroz et al. 2019) through either the PyMultiNest package (Buch-

ner et al. 2014) or the *dynesty* package (Speagle 2019). We adopted PyMultiNest in this work.

We first fitted a Gaussian Process (GP) with a Matern kernel to the data with the transit windows masked. The adjustable parameters and their priors along with the best-fit values are listed in Table 3. The best-fit value corresponds to the median of the posterior distribution, with the lower and upper limits being defined by the 16th and 84th percentiles of the posterior distribution, respectively. The same applies throughout the rest of the paper. We set uniform priors with widths of one day for the planet orbital period ( $P_b$ ) and the time of conjunction ( $t_{0,b}$ ) according to the values provided on ExoFOP, which are wide enough to not influence the results and can save the computational time compared to infinitely wide ones. The stellar density was estimated by the SED fitting and therefore received a normal prior centered at 1719.4 kg/m<sup>3</sup> with  $\sigma = 212.6$ . We adopted a new parameterization of  $r_{1,b}$  and  $r_{2,b}$  with a uniform prior between 0 to 1 to fit the planet-to-star radius ratio  $p = R_b/R_\star$  and the impact parameter  $b = (a_b/R_\star) \cos i_b$ , which follows the relations in the algorithm proposed by Espinoza (2018). This new parameterization and sampling will explore all the physically meaningful ranges for  $p$  and  $b$  in the  $(b, p)$  plane and meanwhile meet the condition of  $b < 1 + p$ .

We floated the eccentricity  $e_b$  and the argument of periapsis  $\omega_b$  to test if the photometry could provide any constraint on the planet’s eccentricity. For  $e_b$  and  $\omega_b$  we gave wide, uninformative priors,  $\mathcal{U}(0, 1)$  and  $\mathcal{U}(0, 360^\circ)$ . No obvious evidence for an eccentric orbit was found and  $e_b$  converged towards zero with the value of  $0.10^{+0.10}_{-0.07}$ . The Bayesian model log-evidence  $\ln Z$  between the circular and eccentric orbit models were compared following Trotta (2008). We judge whether one model is more favored than the other by considering  $2 \leq \Delta \ln Z < 5$  as moderate evidence and  $\Delta \ln Z \geq 5$  as strong evidence. In our case,  $\ln Z$  of a circular orbit model is  $\sim 2.3$  larger than the eccentric one. Given the small period of planet b, we also expect that tidal force might have damped the eccentricity to below a detectable level of *TESS* light curves. We thus adopted  $e_b \equiv 0$ .

In principle, the PDCSAP file was already removed the flux contamination from other stars in the nearby pixels, but considering the contamination ratio estimated by TICv8 is relatively large (0.1) for this target, we floated the *TESS* photometric dilution factor  $D_{\text{TESS}}$  with a normal prior centered around 1.0 with a standard deviation of 0.1. This parameter converged to the value of  $0.98 \pm 0.09$ , so it was then fixed to 1.0 in the following TTV analysis (Section 4.1.2). We gave uniform pri-

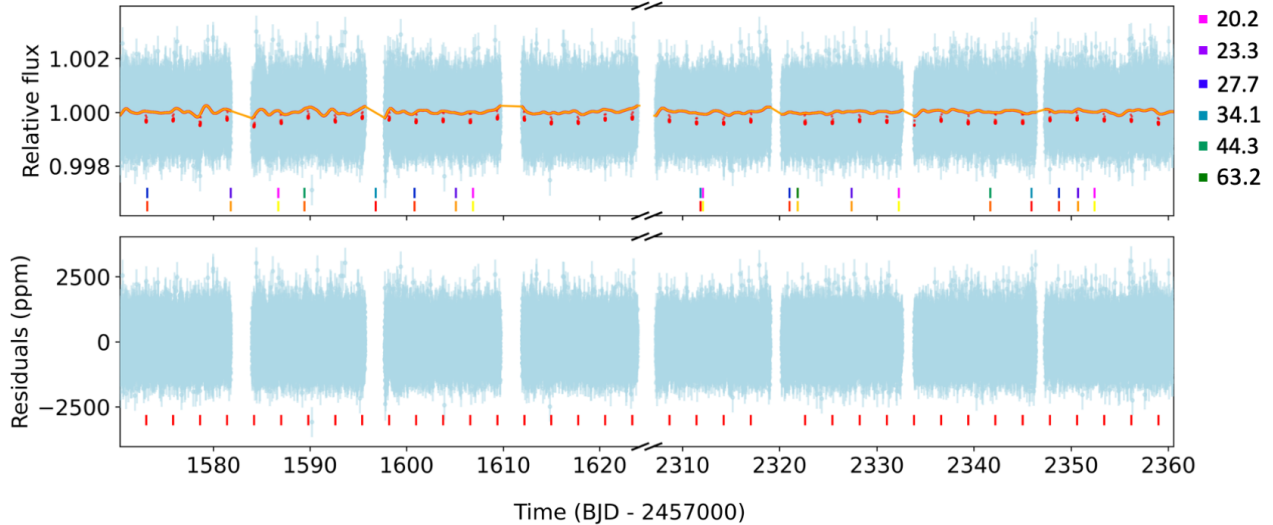


**Figure 5.** Top panel: *TESS* light curve and our best-fit detrending and transit model for planet b, with illustrations of the possible transit ephemerides of the planet candidate. The orange solid line corresponds to the detrending model using GP, while the transit fitting results are marked in red. The short vertical lines near the bottom illustrate the most probable transit ephemerides of the candidate based on the MAP grid search from *RadVel* (see 4.2.1). Each probable set of ephemerides is marked with two sets of vertical lines: the top set of magenta to cyan colors correspond to an increasing period value as labeled on the right, while the bottom set of yellow to red corresponds to an increasing MAP value. Bottom panel: Residuals of the photometric fit. In this panel only the transit events of planet b are marked with small red vertical lines. Note that the time-axis is not continuous as there is a 683-day gap with no *TESS* measurements.

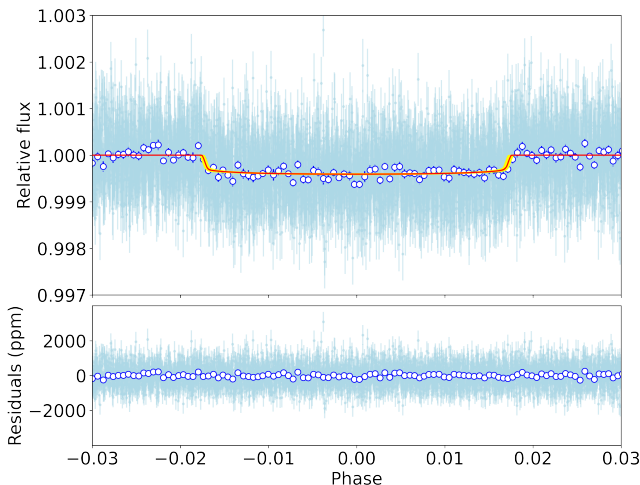


**Figure 6.** Phase-folded *TESS* light curve (light blue) and the best-fit transit model (red line with yellow 1- $\sigma$  band) for planet b, with the residuals plotted in the lower panel. The big circular points show the binned photometry with 40 data points in each bin.

ors  $\mathcal{U}(0,1)$  to the quadratic limb darkening coefficients  $q_{1,\text{TESS}}$  and  $q_{2,\text{TESS}}$ .

Figure 5 and 6 show our fitting results. We obtained a planet period of 2.797 days for TOI-784b, which is consistent with the *TESS* provided value. Combining with the stellar radius in Section 3.1, we derived the

planet radius  $R_b$  to be  $1.93^{+0.11}_{-0.09} R_{\oplus}$  from the best-fit values of  $b$  and  $p$ .

#### 4.1.2. TTV Analysis

After detrending the light curves of TOI-784, we also checked if the system has Transit-Timing Variation (TTV) signals using *Juliet*. We applied the *dynesty* package this time for higher computational efficiency. There are 20 transits in the first year (2019) and 18 transits in 2021. The ninth transit observed in 2021 was partiality captured at the beginning of Sector 38, and thus was excluded in the following analyses. The planet period  $P_b$  and transit epoch  $t_{0,b}$  used to calculate the ephemeris for each transit comes from the transit modeling on the *TESS* photometry in the previous subsection, which gives us  $P_b = 2.797$  days and  $t_{0,b} = 2336.6$  (BJD-2457000). We set a normal prior for each transit ephemeris that centered at the corresponding best-fitted time of conjunction with the standard deviation of 0.01. Other parameters' priors remain the same as in Section 4.1.1 except the *TESS* photometric dilution factor  $D_{\text{TESS}}$ , which we simply fixed to one for efficiency concern.

We do not find any convincing evidence of TTV in our results. The O-Cs range from about 0.2 to 13.5 minutes with no periodic feature as shown in Figure 7. This is as expected given our estimates on the possible orbital solutions and mass for the planet candidate (see Sec-

**Table 3.** Priors, best-fit values, and derived parameters of *TESS* photometry analysis

Parameter	Prior	Best-fit	Description
<i>Detrending parameters</i>			
$D_{\text{TESS}}$	Fixed	1	<i>TESS</i> photometric dilution factor
$M_{\text{TESS}}$	$\mathcal{N}(0, 0.1^2)$	$0.00010^{+0.000096}_{-0.000094}$	Mean out-of-transit flux of <i>TESS</i> photometry
$\sigma_{\text{TESS}}$ (ppm)	$\mathcal{J}(10^{-6}, 10^6)$	$172.76^{+4.80}_{-4.69}$	Extra photometric jitter term of <i>TESS</i> light curve
$\sigma_{\text{GP,TESS}}$ (ppm)	$\mathcal{J}(10^{-6}, 10^6)$	$0.00049^{+0.000029}_{-0.000015}$	Amplitude of the Gaussian Process
$\rho_{\text{GP,TESS}}$	$\mathcal{J}(10^{-3}, 10^3)$	$2.52^{+0.16}_{-0.11}$	Length scale of the Gaussian Process
<i>Transit parameters</i>			
$P_b$ (day)	$\mathcal{U}(2.3, 3.3)$	$2.7970365^{+0.0000031}_{-0.0000030}$	Orbital period of TOI-784b
$t_{0,b}$ (BJD-2457000)	$\mathcal{U}(2336.1, 2337.1)$	$2336.61221^{+0.000044}_{-0.000050}$	Time of transit-center for TOI-784b
$r_{1,b}$	$\mathcal{U}(0, 1)$	$0.480^{+0.081}_{-0.088}$	Parametrisation for p and b
$r_{2,b}$	$\mathcal{U}(0, 1)$	$0.0195^{+0.0010}_{-0.0009}$	Parametrisation for p and b
$e_b$	Fixed	0	Orbital eccentricity of TOI-784b
$\omega_b$	Fixed	90	Argument of periapsis of TOI-784b
$\rho_*$ (kg/m <sup>3</sup> )	$\mathcal{N}(1719.4, 212.6^2)$	$1781^{+111}_{-178}$	Stellar density
<i>TESS photometry parameters</i>			
$q_{1,\text{TESS}}$	$\mathcal{U}(0, 1)$	$0.10^{+0.13}_{-0.07}$	Quadratic limb darkening coefficient
$q_{2,\text{TESS}}$	$\mathcal{U}(0, 1)$	$0.28^{+0.35}_{-0.21}$	Quadratic limb darkening coefficient
$D_{\text{TESS}}$	$\mathcal{N}(1, 0.1^2)$	$0.981^{+0.090}_{-0.086}$	<i>TESS</i> photometric dilution factor
$M_{\text{TESS}}$	$\mathcal{N}(0, 0.1^2)$	$-0.0000015^{+0.0000022}_{-0.0000021}$	Mean out-of-transit flux of <i>TESS</i> photometry
$\sigma_{\text{TESS}}$ (ppm)	$\mathcal{J}(0.1, 1000)$	$158.8^{+5.5}_{-5.4}$	Additional photometric jitter term of <i>TESS</i>
<i>Derived planetary parameters</i>			
$a_b/R_*$	—	$9.03^{+0.18}_{-0.31}$	Scaled semi-major axis of the orbit for TOI-784b
$b_b$	—	$0.22^{+0.12}_{-0.13}$	Impact parameter of the orbit for TOI-784b
$p_b$	—	$0.0195^{+0.0010}_{-0.0009}$	Planet-to-star radius ratio
$i_b$ (°)	—	$88.60^{+0.84}_{-0.86}$	Orbital inclination of TOI-784b

tion 4.2). We estimated the possible Hill radii of the candidate using the equation:  $r = a_c(1 - e_c)[m_c/(3M_*)]^{1/3}$  (Hamilton & Burns 1992), and we found that the maximum Hill sphere radius of planet candidate c is  $r_{H,c} \sim 0.011$  AU, corresponding to only  $0.041(a_c - a_b)$  given  $a_b \sim 0.038$  AU. The average ratio between  $r_{H,c}$  and the separation of the two planets ( $a_c - a_b$ ) is about 0.035 over the six possible solutions of planet candidate c found in RadVel, which means that the second planet is too far away from planet b to cause any significant TTV.

#### 4.2. RV analysis - Possible solutions of a two-planet fit

Modeling the RV data taken by Magellan/PFS with a single transiting planet leaves a clear residual beyond the estimated level of stellar jitter ( $\lesssim 1.2$  m/s; see Appendix A). This can be seen in Figure 16, which displays an example of the one-planet RV fit and shows clear residuals after subtracting the signals from planet b (in panel b). This trend is unlikely to be caused by instrumental systematics, since a significant linear trend like this, as large as  $\sim 5$  m/s in ten days, has not been observed in the RVs of any standard stars observed by

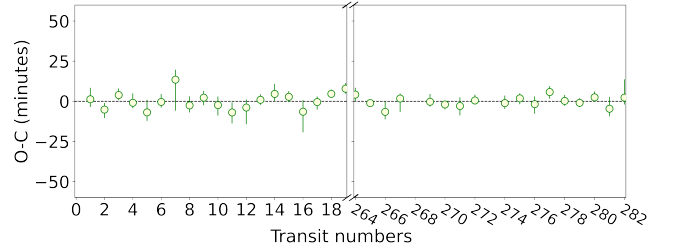


**Figure 7.** The  $O-C$  diagram of the TTV analysis, showing the timing of the transit mid-point for each epoch. In total there were 36 transits in our TTV analysis using *juliet*. We found no apparent TTV signals.

PFS. For example, PFS's RVs on Tau Ceti (HD 10700) have a standard deviation of less than 2 m/s in four years. Therefore, we incorporated a second planet in our RV model.

We performed a joint fit of the two-year PFS data along with NRES and CHIRON data using RadVel. However, due to the limited RV data timespan, we could not map out the entire orbit of the second planet. The maximum a posteriori (MAP) solution for the second

planet’s orbit is quite sensitive to the specific initial guesses for its RV semi-amplitude  $K_c$  and orbital period  $P_c$ , and afterward, the results of the Markov Chain Monte Carlo (MCMC) analysis will fall into local minimums. As two out of three sections of PFS data appear to capture the same phase of the second planet’s orbit (see Figure 16), the degeneracy between  $P_c$  and  $K_c$  is not surprising. Therefore, we explore the parameter space for the potential second planet and provide a suite of best estimates for the orbital solution of this planet candidate.

In this section, we explore the  $(P_c, K_c)$  parameter space using both *RadVel* and *Juliet* to identify potential orbital solutions for the planet candidate. Initially, we utilized the NRES and CHIRON RVs along with the PFS RVs to place an upper limit on the RV semi-major amplitude for the planet candidate, excluding the possibility of a brown dwarf. Therefore, we took four more RV observations with PFS in March 2022. With the new data at hand, we found that the possible solutions are primarily determined by the PFS RVs. To help the nested sampling converge in *Juliet* and simplify our model, we excluded the NRES and CHIRON RVs from subsequent analyses.

Although we only use PFS data, we include an example of a two-planet fit that uses data from all three instruments in Figure 8 for completeness. Additionally, we present our fits assuming only planet b’s signal along with some other non-Keplerian signals (such as additional RV trends or a generic Gaussian Process model) in Appendix A.

Table 4 presents a model comparison of different radial velocity (RV) models using the Bayesian information criterion (BIC) and the second-order Akaike information criterion ( $AIC_c$ ). Both BIC and  $AIC_c$  are statistical model selection criteria used to assess the fit of a model to a given dataset.  $AIC_c$  is a corrected version of AIC that accounts for sample size. Lower values of  $AIC_c$  and BIC indicate a better model fit. According to the *RadVel* manual, we consider that we can not distinguish the goodness of two models when  $\Delta AIC_c$  is less than 2; we consider that one is slightly more favoured with  $\Delta AIC_c$  between 2 to 4; we consider that one is strongly disfavoured with  $\Delta AIC_c$  between 4 to 10; and we consider that one can be ruled out when  $\Delta AIC_c$  is greater than 10. Using these criteria, we compared the one-planet fit assuming a circular or eccentric orbit for planet b and found that the former is more favored. Thus, we applied the circular orbit and compared the one-planet fit versus the two-planet fit. We will discuss the two-planet fit in the following sections. We also incorporated a generic Gaussian process (GP) model to

replace the linear trends in the one-planet fit, which is found to be strongly disfavored by the data.

#### 4.2.1. Two-planet fit in *RadVel*

We performed a grid search using the maximum a posteriori (MAP) fit method in *RadVel*. We constructed a grid of parameters in the  $(P_c, K_c)$  space, and for each fixed set of  $P_c$  and  $K_c$  values, we performed a MAP fit using *RadVel* with  $P_b$ ,  $t_{0,b}$ ,  $t_{0,c}$ , and the velocity zero points and jitters as the free parameters. The results are shown in Figure 9, where we color-coded the MAP values for each MAP fit using a set of  $(P_c, K_c)$  in the grid. We detail our choices for the priors and the  $(P_c, K_c)$  grid in the next two paragraphs. The most likely solutions of  $(P_c, K_c)$  are marked in red in Figure 9, corresponding to a  $\ln(\text{MAP})$  difference within 5 (roughly  $\Delta AIC_c \leq 10$ ) compared to the highest one.

The prior distributions for the free parameters are summarized in Table 5. We gave normal distributions for  $P_b$  and  $t_{0,b}$  centered at the best-fit values from the photometry analysis with widths set to one order of magnitude larger than the corresponding error bar reported by the photometry. For the planet candidate, we assumed a circular orbit, and we estimated an initial guess for  $t_{0,c} \sim \text{BJD } 2458920$  by examining the residual RVs in the one-planet fit and estimating the RV zero-crossing going from redshift to blueshift (see Appendix A and Figure 16).

For the  $(P_c, K_c)$  grid, we first mapped out a wider range of (5,1) (in days and m/s, respectively) to (2000,200) and found no plausible solutions beyond  $\sim 60$  m/s and 300 days. We thus narrowed down the grid to a range of (5,1) to (300,60) (days, m/s). In order to perform a smoother and more careful search around the left corner region of the  $(P_c, K_c)$  space where a larger MAP value appears (red dots in Figure 9), we divided the parameter space into log-uniform grids with 600 and 150 points along the  $P_c$ - and  $K_c$ -axis, respectively. We also created a more concentrated uniformly distributed grid with 0.05 m/s and 0.1 day interval on the region of (5,1) to (100,20) (gray dashed lines framed in Figure 9) to verify that varying the density of the grid will not result in additional islands of the possible solutions.<sup>9</sup>

<sup>9</sup> We would get more  $(P_c, K_c)$  pairs falling into the red regions in Figure 9, naturally, if we choose a higher resolution for the grid, but the results should not differ in any significant way with the current grid. It is also unlikely that there would be new islands of  $(P_c, K_c)$  pairs with high MAP values, since our MAP results using *RadVel* are consistent with the posterior space we mapped out using *Juliet* in the following subsection.

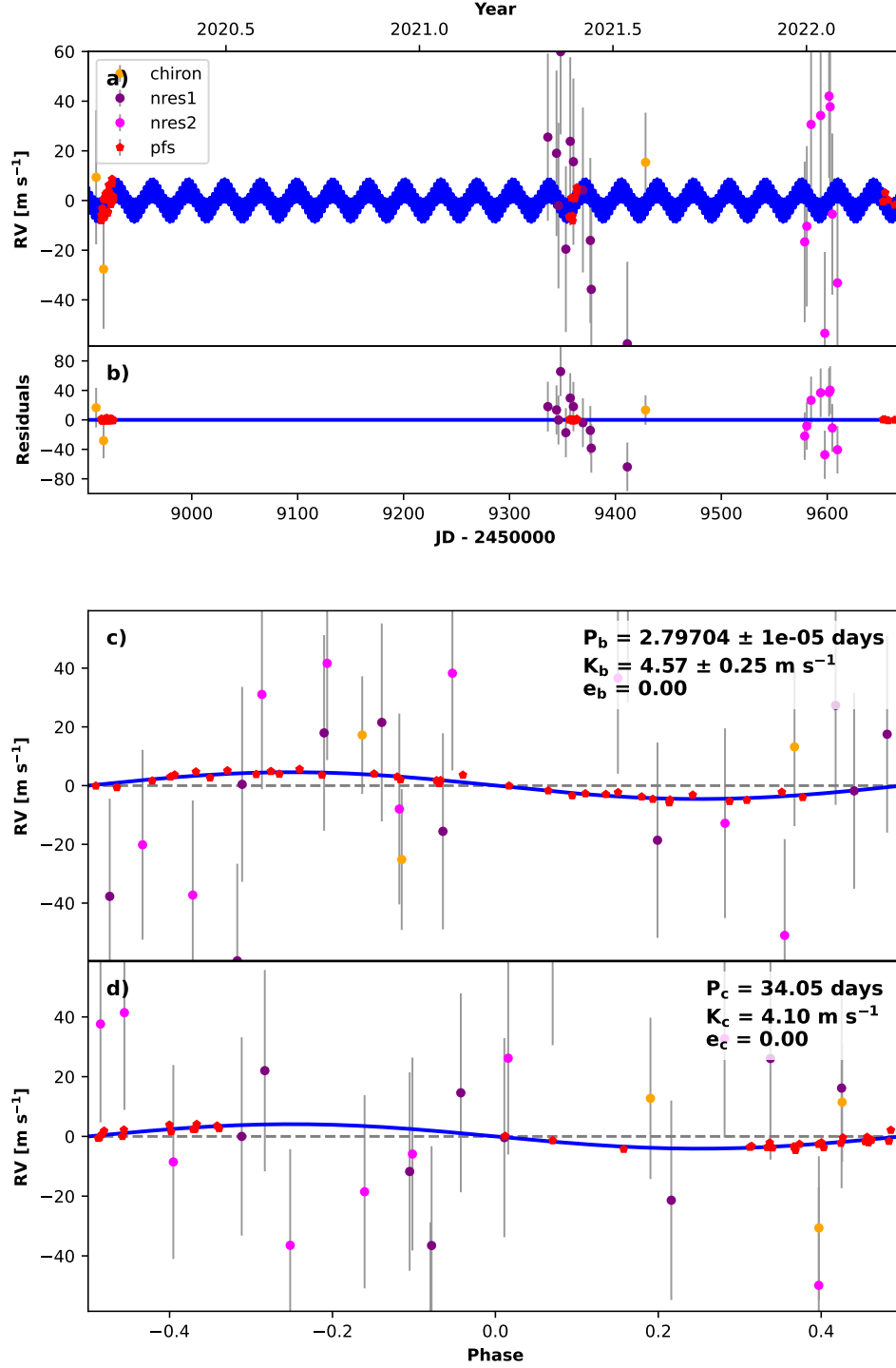


**Figure 8.** An example of the two-planet Keplerian orbital model. The period  $P_c$  and RV semi-amplitude  $K_c$  are fixed at 34.05 days, 4.1 m/s, respectively, which is the solution with the highest MAP value among our MAP grid search (see Section 4.2.1). RVs from different instruments are marked with different colors following previous plots: red – PFS, purple and magenta – NRES (indices of 1 and 2 represent facilities in South African Astronomical Observatory and Cerro Tololo Interamerican Observatory, respectively), and yellow – CHIRON.

In summary, six most likely values of  $P_c$  have been revealed:  $\sim 20, 23, 28, 34, 44,$  and  $63$  days<sup>10</sup>. The MAP value of the 63-day solution is more sensitive to the chosen grid, i.e. the inputted  $(P_c, K_c)$  values compared to others, which illuminates that it should be a less stable or shallower local minimum (see also Section 4.2.2). We list the six  $(P_c, K_c)$  combinations with the highest MAP values in each group along with the derived  $M_c \sin i_c$  and the corresponding  $\ln(\text{MAP})$  values in Table 7.  $K_b$  has an average of 4.7 m/s over the most possible solutions in the red islands of Figure 9, which is consistent with the one-planet fit we discussed in Appendix A within the  $1\sigma$  level. This consistency demonstrates that the constraint on planet b’s mass is insensitive to the orbital solution of the planet candidate.

#### 4.2.2. Two-planet fit in *Juliet*

We also performed a two-planet fit using *Juliet* with the same priors as in our *RadVel* grid search, except for  $K_c$  and  $P_c$ , where we adopted uniform priors of  $\mathcal{U}(0, 60)$  and  $\mathcal{U}(10.0, 450.0)$  (see Table 6). Figure 10 shows the corner plot of the marginalized posterior distributions of  $K_b, P_b, K_c$  and  $P_c$  (a complete version with all variables included is shown in Figure 21). The lower panel of Figure 10 is an enlarged plot of  $P_c - K_c$ ’s posterior space along with the corresponding histogram for each parameter. There are six peaks in the posterior distribution of  $P_c$ , which are at consistent values as the six groups we obtained in the *RadVel* MAP grid search (Section 4.2.1).

We should note that the relative height of each possible  $P_c$  in the histogram, i.e. the number of points in each island in the posterior space (orange circles in Figure 10, hereafter posterior samples) do not reflect the relative probability for each solution. The fraction of posterior samples for each possible  $P_c$  varies between runs even if we set the same priors and same settings for the nested sampling (including the number of live points  $n_{\text{live}}$ <sup>11</sup>). We checked the results for runs with 500, 1000, 2000, 3000, 4000, 5000, and 6000 live points and found that in general, more posterior samples were mapped out around each possible  $(P_c, K_c)$  pair with an increasing

number of live points. The five islands of the  $(P_c, K_c)$  pair from 20-44 days emerge significantly more clearly in the marginalized posterior distributions after  $n_{\text{live}}$  was increased to 1000, while the posterior samples around the 63-day solution only appeared when  $n_{\text{live}} = 5000$ , which may imply that this solution is rather unstable or has a narrower or shallower local minimum in the posterior space. Since we also found the 63-day solution in the MAP grid search using *RadVel*, we adopted  $n_{\text{live}} = 5000$  and present the results in Figure 10.

Though the relative probability of these six posterior peaks is unreliable (e.g., Salomone et al. 2018), the distribution within each local minimum should be trustworthy. We thus did a more concentrated search in the posterior space around each solution with *Juliet* to estimate the uncertainties of  $P_c$  and  $K_c$  of the six possible solutions. To be specific, for each of the six solutions, we set a uniform prior for  $P_c$  around each solution with a width wide enough to fully cover this local minimum and away from other nearby local minimums. We also verified that varying the choice of the prior width did not affect the final posterior for each local minimum as long as the width is wide enough (e.g. one order of magnitude larger than the posterior range). The six possible solutions for the planet candidate and their estimated uncertainties from the individual posterior distributions are reported in Table 7. The phase-folded plots of the planet candidate are shown in Figure 11, with each sub-panel showing the results of a MAP fit using  $(P_c, K_c)$  fixed at each possible solution as listed in Table 7.

The orbital solution for planet b is also presented in Figure 10. We derived the posterior distributions for  $M_b$  and  $a_b$  from the orbital parameters of planet b and the stellar parameters of TOI-784, which resulted in a median  $M_b \sin i_b$  of  $9.67 M_{\oplus}$  and  $a_b$  of 0.04 AU. These values are also consistent with what we found in the one-planet fit (Appendix A) within  $1\sigma$ . Considering  $i_b$  derived from the transit fit which is  $88.60^{+0.84}_{-0.86}$ , we calculated the mass for planet b  $M_b$  to be  $9.67^{+0.83}_{-0.82} M_{\oplus}$ .

We present the properties of planet b and the planet candidate obtained from both photometry (Section 4.1) and RV analyses (Section 4.2) in Table 8.

We compare the two-planet fit with other model settings in Table 4. As discussed in the preceding sections, the planet candidate has multiple orbital solutions. We report the BIC and  $\text{AIC}_c$  values of the model with the highest MAP value, where  $P_c$  and  $K_c$  were fixed at 34.05 days and 4.1 m/s, respectively (see Table 7). While the model of one-planet fit with the circular orbit assumption plus trends has a lower  $\text{AIC}_c$  than the two-planet fit, we cannot consider it the most favored model,

<sup>10</sup> The same analysis was performed using joint RVs from both PFS, NRES and CHIRON for completeness, in which we found the same six best sets of  $P_c$  and  $K_c$  as expected.

<sup>11</sup> We applied the nested sampling implemented via *PyMultiNest* based on the MultiNest algorithm as described in Section 4.1.1. The live point stands for a series of test points uniformly distributed within the given prior for each variable parameter at the beginning, and they are then kept or rejected according to their *likelihood* (see e.g. Feroz et al. 2009 for a detailed description).

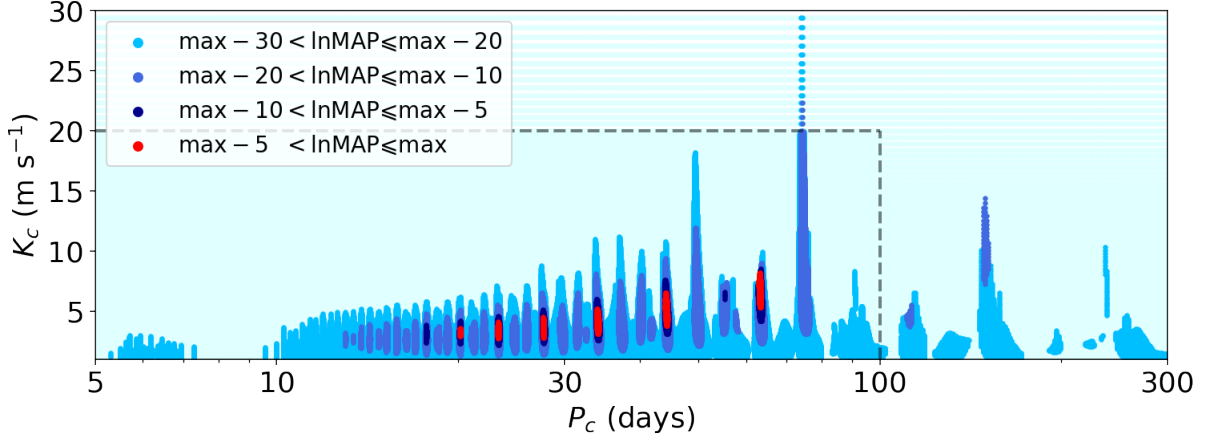


**Figure 9.** The  $\ln(\text{MAP})$  values of a MAP grid search in the  $(P_c, K_c)$  space using **RadVel**. Grids placed in a log-uniform distribution were applied along  $P_c$  and  $K_c$  axes. The region framed by gray dashed lines was also mapped with another uniformly distributed grid with a smaller interval. As informed in the upper-left legend, different ranges of  $\ln(\text{MAP})$  values are marked by different colors. We treat the periods whose  $\ln(\text{MAP})$  values differ by five from the highest  $\ln(\text{MAP})$  value to be “the most possible solutions” of the planet candidate. The cyan region is the least favored solution with  $\ln(\text{MAP})$  differences larger than 30. We also explored the  $K_c$  space between 30 and 60 m/s but did not find any plausible solutions, hence it is not plotted here.

**Table 4.** Comparison of different RV fitting models\*

Model	BIC	AIC <sub>c</sub>	$\Delta\text{AIC}_c$	Description
1pl-circular + trend	116.07	111.15	-1.23	One-planet, circular orbit, two trends
1pl-eccentric + trend	121.70	118.36	5.98	One-planet, eccentric orbit, two trends
1pl-circular + GP	159.06	152.27	39.89	One-planet, circular orbit, GP model
2pl-circular	118.71	112.38	0	Two-planet, circular orbits for both

NOTE—\* Only PFS data were used in the fittings.

since the combination of two linear trends is artificially included and non-physical.

#### 4.3. Does planet candidate *c* transit?

Based on the possible  $(P_c, K_c)$  provided in Section 4.2, we derived the corresponding  $M_c \sin i_c$  values and then estimated the corresponding radius,  $R_c$  values, based on an empirical M-R relation with the python package **MRExo** (Corrales 2015). We estimated the transit depths and durations using Equation (3) in Seager & Mallén-Ornelas (2003). Overall, the transit depth is typically larger than 900 ppm and the duration can last for at least 4.8 hours.

Comparing the derived transit depths and durations with those of TOI-784b, whose depth and duration are roughly 400 ppm and 2.4 hours, there should be an evident signal in the *TESS* photometry assuming planet candidate *c* transits and has the best-fit parameters we found in the two-planet RV fits (Section 4.2). In order

to quantify the null detection of the *c*’s transit, we performed an injection-and-recovery test based on the algorithm used in Gan et al. (2022). We injected a series of transit signals into the detrended *TESS* light curve with various sets of values for the period  $P_i$  and radius  $R_i$  of the planet candidate. We chose the ranges of  $P_i$  and  $R_i$  to cover the possible solutions we described in Section 4.2 with  $P_i = [18, 66]$  days and  $R_i = [2.8, 6.4] R_\oplus$ . We divided the parameter space of  $P_i$  and  $R_i$  into a 21 by 21 grid, with each bin covering a  $\Delta P_i$  of 2.4 days and  $\Delta R_i$  of  $0.18 R_\oplus$ . In each bin, we generated 100 sets of random  $P_i$  and  $R_i$  values with random orbital phases to create the synthetic transit signals and inject them into the detrended *TESS* light curve of TOI-784. We then searched for any periodic signal between 15 and 70 days with a 0.01-day grid using the Box Least Squares (BLS) method (Kovács et al. 2002). This criterion is feasible because we can successfully find TOI-784b whose depth and duration are much smaller using the same criterion.

**Table 5.** Priors for the two-planet fit MAP grid search using *RadVel*

Parameter	Prior	Description
$P_b$ (day)	$\mathcal{N}(2.7970364, 0.00001^2)$	Orbital period of TOI-784b
$t_{0,b}$ (BJD)	$\mathcal{N}(2459336.61220, 0.001^2)$	Time of transit-center for TOI-784b
$\sqrt{e_b} \sin \omega_b$	Fixed to 0	
$\sqrt{e_b} \cos \omega_b$	Fixed to 0	
$K_b$ (m/s)	$\mathcal{U}(-20.0, 20.0)$	RV semi-amplitude of TOI-784b
$P_c$ (day)	Fixed	Orbital period of the planet candidate
$t_{0,c}$ (BJD)	$\mathcal{U}(2457000.0, 3457000.0)$	Time of transit-center for the planet candidate
$\sqrt{e_c} \sin \omega_c$	Fixed to 0	
$\sqrt{e_c} \cos \omega_c$	Fixed to 0	
$K_c$ (m/s)	Fixed	RV semi-amplitude of the planet candidate
$\dot{\gamma}$	Fixed to 0	Linear trend term in the RV fit
$\ddot{\gamma}$	Fixed to 0	Curvature term in the RV fit
$\mu_{\text{PFS}}$	$\mathcal{N}(0.0, 10.0^2)$	Velocity zero-point for PFS
$\mu_{\text{NRES1}}$	$\mathcal{N}(15100.0, 100.0^2)$	Velocity zero-point for NRES1
$\mu_{\text{NRES2}}$	$\mathcal{N}(14800.0, 100.0^2)$	Velocity zero-point for NRES2
$\mu_{\text{CHRION}}$	$\mathcal{N}(15700.0, 100.0^2)$	Velocity zero-point for CHRION
$\sigma_{\text{PFS}}$	$\mathcal{U}(0.0, 15.0)$	Jitter term for PFS
$\sigma_{\text{NRES1}}$	$\mathcal{U}(0.0, 60.0)$	Jitter term for NRES1
$\sigma_{\text{NRES2}}$	$\mathcal{U}(0.0, 60.0)$	Jitter term for NRES2
$\sigma_{\text{CHRION}}$	$\mathcal{U}(0.0, 60.0)$	Jitter term for CHRION

**Table 6.** Priors and best-fit values of the two-planet fit using *Juliet*

Parameter	Prior	Best-fit	Description
$P_b$ (day)	$\mathcal{N}(2.7970409, 0.00001^2)$	$2.7970343^{+0.0000063}_{-0.0000063}$	Orbital period of TOI-784b
$t_{0,b}$ (BJD)	$\mathcal{N}(2459336.61220, 0.001^2)$	$2459336.61221^{+0.00059}_{-0.00073}$	Time of transit-center for TOI-784b
$\sqrt{e_b} \sin \omega_b$	Fixed	0	
$\sqrt{e_b} \cos \omega_b$	Fixed	0	
$K_b$ (m/s)	$\mathcal{U}(-20.0, 20.0)$	$4.67^{+0.20}_{-0.19}$	RV semi-amplitude of TOI-784b
$P_c$ (day)	$\mathcal{U}(10.0, 450.0)$	$44.30^{+0.07}_{-0.06}$	Orbital period of the planet candidate
$t_{0,c}$ (BJD)	$\mathcal{U}(2457000.0, 3457000.0)$	$3079945^{+210953}_{-273077}$	Time of transit-center for the planet candidate
$\sqrt{e_c} \sin \omega_c$	Fixed	0	
$\sqrt{e_c} \cos \omega_c$	Fixed	0	
$K_c$ (m/s)	$\mathcal{U}(0.0, 60.0)$	$4.64^{+0.34}_{-0.41}$	RV semi-amplitude of the planet candidate
$\mu_{\text{PFS}}$	$\mathcal{N}(0.0, 10.0^2)$	$0.04^{+0.36}_{-0.40}$	Velocity zero-point for PFS
$\sigma_{\text{PFS}}$	$\mathcal{U}(0.0, 15.0)$	$0.87^{+0.20}_{+0.17}$	Jitter term for PFS

We define an injected synthetic planet as “recovered” when the period with the highest S/N reported by the BLS search is within 0.05% from the injected period and its harmonics (1/2 or integers) are with S/N > 10.

Due to the longer period of the planet candidate and the relatively short baseline of the *TESS* coverage separated by a two-year gap (2 sectors spanning 55 days in 2019, and another two sectors in 2021), the detection completeness is sensitive to the total number of transits within the *TESS* coverage, as shown in Figure 12. The typical number of transits  $N_t$  for each  $P_i$  bin is estimated

by taking the average of the numbers of transits in the corresponding simulated transit injections.

We also performed injection-and-recovery tests for each possible period (yellow lines in Figure 12), incorporating the phase information on  $t_{0,c}$  from the RV data, using the same strategy as described above. The injected periods  $P_i$  were randomly picked out with a corresponding  $K_i$  from the marginalized  $P_c - K_c$  posterior distribution we obtained from *Juliet* (Section 4.2.2). We then estimated the corresponding time of transit-center  $t_{0,i}$  for the selected ( $P_c, K_c$ ) pair using the MAP

**Table 7.** Possible solutions of TOI-784 c found in *RadVel* and *Juliet*

$K_c$ (m/s)	$P_c$ (day)	$a_c$ (AU)	$M_c \sin i_c$ ( $M_\oplus$ )	$\ln(\text{MAP})$ values
<i>RadVel</i>				
3.20	20.15	0.14	12.79	-59.45
3.40	23.30	0.15	14.26	-56.53
3.60	27.70	0.17	16.00	-55.59
4.10	34.05	0.20	19.51	-55.52
5.06	44.25	0.24	26.28	-56.21
7.00	63.20	0.30	40.95	-57.23
<i>Juliet</i>				
$3.16^{+0.24}_{-0.24}$	$20.128^{+0.017}_{-0.018}$	$0.14^{+0.00}_{-0.01}$	$12.6^{+1.4}_{-1.3}$	—
$3.31^{+0.23}_{-0.24}$	$23.310^{+0.023}_{-0.022}$	$0.15^{+0.01}_{-0.01}$	$13.8^{+1.4}_{-1.4}$	—
$3.51^{+0.25}_{-0.26}$	$27.682^{+0.033}_{-0.030}$	$0.17^{+0.01}_{-0.01}$	$15.5^{+1.6}_{-1.6}$	—
$3.98^{+0.26}_{-0.28}$	$34.065^{+0.045}_{-0.042}$	$0.20^{+0.01}_{-0.01}$	$18.9^{+2.0}_{-1.9}$	—
$4.68^{+0.38}_{-0.40}$	$44.296^{+0.069}_{-0.065}$	$0.24^{+0.01}_{-0.01}$	$24.2^{+2.8}_{-2.7}$	—
$5.35^{+0.43}_{-0.56}$	$63.393^{+0.135}_{-0.110}$	$0.30^{+0.01}_{-0.01}$	$31.1^{+3.6}_{-3.9}$	—

**Table 8.** Composite parameters for planet b and planet candidate c from photometry and RV analyses

Parameter	Value
Planet b	
$t_{0,b}$ (BJD-2457000)	$2336.61221^{+0.00044}_{-0.00050}$
$P_b$ (day)	$2.7970365^{+0.0000031}_{-0.0000030}$
$K_b$ (m/s)	$4.67^{+0.20}_{-0.19}$
$e_b$	Fixed to 0
$a_b$ (AU)	$0.038^{+0.001}_{-0.001}$
$M_b$ ( $M_\oplus$ )	$9.67^{+0.83}_{-0.82}$
$R_b$ ( $R_\oplus$ )	$1.93^{+0.11}_{-0.09}$
$i_b$ ( $^\circ$ )	$88.60^{+0.84}_{-0.86}$
$\rho_b$ (g/cm <sup>3</sup> )	$7.4^{+1.4}_{-1.2}$
The planet candidate	
$P_c$ (day)	20, 23, 28, 34, 44, 63
$K_c$ (m/s)	3.2 – 5.4 from <i>Juliet</i>
$e_c$	Fixed to 0
$a_c$ (AU)	0.14 – 0.30
$M_c \sin i_c$ ( $M_\oplus$ )	12.6 – 31.1
$i_c$ ( $^\circ$ )	$\leq 88.3 - 89.2$

fit in *RadVel* to include the phase information. The radius of the synthetic planet  $R_i$  was given by a uniform distribution ranging from 2 to 7  $R_\oplus$ . The results of the transit detection possibility as a function of the planet size are shown in Figure 13, which resembles the general trends in Figure 12. The average detection completeness integrated over the whole radius range are 99.9%, 90.4%, 98.9%, 97.8%, 15.0%, and 19.5% for the six possible periods from 20 to 63 days, respectively.

Therefore, the fact that *TESS* did not report a transit detection of planet candidate c suggests that it either does not transit (if having a relatively shorter period)

or its transits escaped *TESS*'s detection due to its long period (if  $P_c > \sim 40$  days). *TESS* will re-observe TOI-784 in Sectors 63-64, in March-May 2023, and additional *TESS* data would provide more leverage to constrain the transit of this planet candidate.

Assuming that the planet candidate does not transit, we can estimate the possible range of its orbital inclination. Our two-planet analysis provided a group of possible values of the semi-major axis  $a_c$  for the planet candidate, with the minimum and maximum values being 0.14 and 0.30 AU. These translate to an orbital inclination of  $i_c \leq 88.3^\circ$  or  $89.2^\circ$ . Compared with the inclination of TOI-784b estimated from the *TESS* light curve,  $88.60^{+0.84}_{-0.86}$ , these two planets could be possibly coplanar even if the second planet does not transit.

## 5. DISCUSSION AND CONCLUSIONS

Properties of planet b and planet candidate c are summarized in Table 8. In Figure 14, we show the mass-radius (M-R) diagram for the sample of confirmed exoplanets (data from TEPCAT database, Southworth 2011) with TOI-784b marked in red.<sup>12</sup> The solid and dashed lines illustrate theoretical models with different compositions according to Zeng et al. (2016), among which Earth composition is estimated with 34% Fe + 66% MgSiO<sub>3</sub>. The M-R relation illuminates that TOI-784b could have a rocky core and presumably no H/He gas envelope. The estimated density of TOI-784b using our measured radius and mass is  $7.4^{+1.4}_{-1.2}$  g/cm<sup>3</sup>, which also suggests that TOI-784b is a super-Earth consis-

<sup>12</sup> The plot was created using the `fancy-massradius-plot` package at <https://github.com/oscaribv/fancy-massradius-plot> by Baragán et al. (2018).

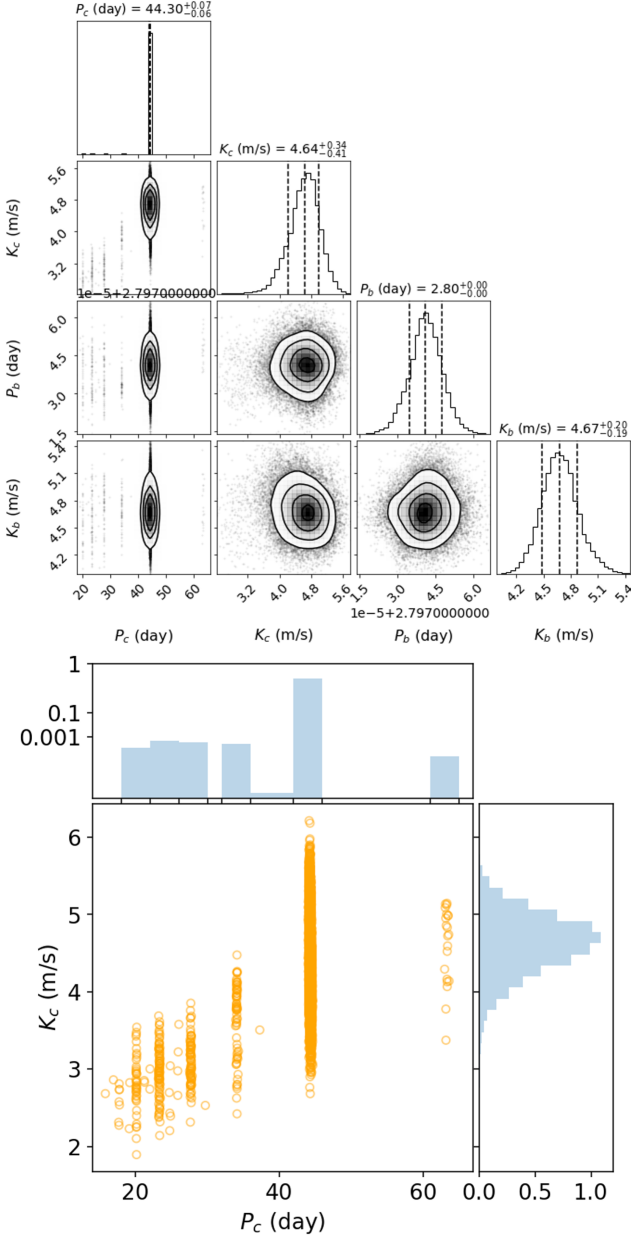


**Figure 10.** Top: The corner plot of the posteriors of partial variable parameters in the two-planet fit using *Juliet* at  $n_{\text{live}} = 5000$ . Bottom: An enlarged version for  $P_c - K_c$ 's posterior space. The histogram of  $P_c$  is plotted on a log scale.

tent with rocky compositions and perhaps no significant atmosphere or ocean. We computed the transmission spectroscopy metric (TSM) and emission spectroscopy metric (ESM) for planet b using Equations (1) and (4) from [Kempton et al. \(2018\)](#). The TSM and ESM values obtained were 36.2 and 6.8, respectively. These values fall below the threshold recommended by [Kempton et al. \(2018\)](#) for high-quality atmospheric characterization targets for a planet with radius of  $1.5 - 10 R_{\oplus}$ , thus may

not suitable for *James Webb Space Telescope (JWST)* to observe. However, planet b may have a small amount of volatile with heavy molecules such as  $\text{H}_2\text{O}$  or  $\text{CO}_2$  instead of  $\text{H}/\text{He}$  given its small size, which is not surprising given its short period and relatively strong stellar irradiation.

We also compared TOI-784b with other super-Earths or sub-Neptunes using data from the NASA Exoplanet Archive<sup>13</sup>. Figure 15 shows the insolation flux  $S_{\text{pl}}$  vs. planet radius  $R_{\text{pl}}$  of TOI-784b in comparison with other known transiting planets. The background contour represents the observed planet number density (not occurrence rate). The dotted line with the  $1\sigma$  error-bar shaded in light green is the empirical relation for the radius valley derived by [Martinez et al. \(2019\)](#), which is consistent with both photoevaporation and core-powered mass-loss models of planet formation. The dashed black line represents the radius valley in a gas-poor formation scenario as predicted by [Lopez & Rice \(2018\)](#).

TOI-784b has a radius of  $1.9^{+0.11}_{-0.09} R_{\oplus}$ , which is at the upper edge of the radius valley ([Fulton et al. 2017](#); [Fulton & Petigura 2018](#)). Various scenarios as mentioned above were proposed to explain this valley. A planet will receive the UV/X-ray flux from its parent star which will erode its gas envelope (photoevaporation). As a consequence, planets on a closer orbit to their hosts experience stronger irradiation and become naked rocky cores, while outer planets tend to keep their envelopes and have a transit radius roughly twice the size of the rocky core ([Owen & Wu 2017](#)). Core-powered mass loss considered the effect of the cooling core, which can also strip envelopes and cause a lack of planets with intermediate radii ([Ginzburg et al. 2018](#); [Gupta & Schlichting 2020](#)). Photoevaporation, as well as the core-powered mass loss scenario, predicts a positive correlation in the insolation flux vs. planet size plane, while gas-poor formation makes an opposite prediction (see Table 5 and Figure 11 in [Cloutier & Menou 2020](#) for a summary) as shown in Figure 15. TOI-784b is located at the lower edge of the radius valley (in the  $R_p - S_p$  plane) predicted by photoevaporation or core-powered mass loss, which is consistent with the atmospheric loss formation scenario considering its rocky composition.

Moreover, the well-separated planet candidate and TOI-784b (period ratio  $> 7$ ) may result from a violent mass loss history ([Wang & Lin 2023](#)). According to previous work on the stability of multi-planet systems with mass loss process, it is possible to keep the

<sup>13</sup> <https://exoplanetarchive.ipac.caltech.edu>, June 21, 2022

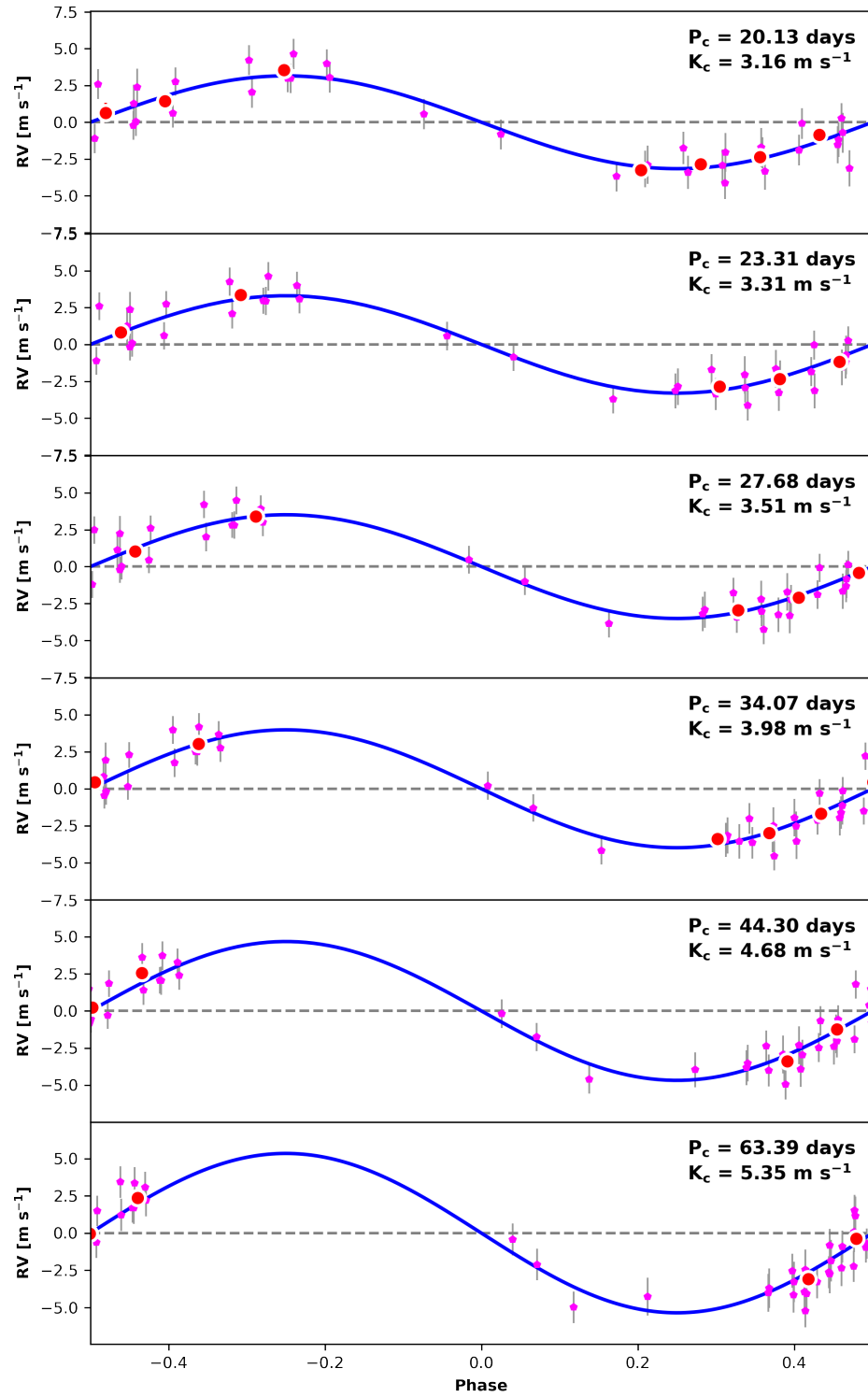


**Figure 11.** Phase-folded RV plots of the planet candidate with the most probable six periods from the two-planet fit in *Juliet*. We assumed a circular orbit for the planet candidate in all cases. PFS RVs are shown in magenta, with the big red dots representing the binned data points.

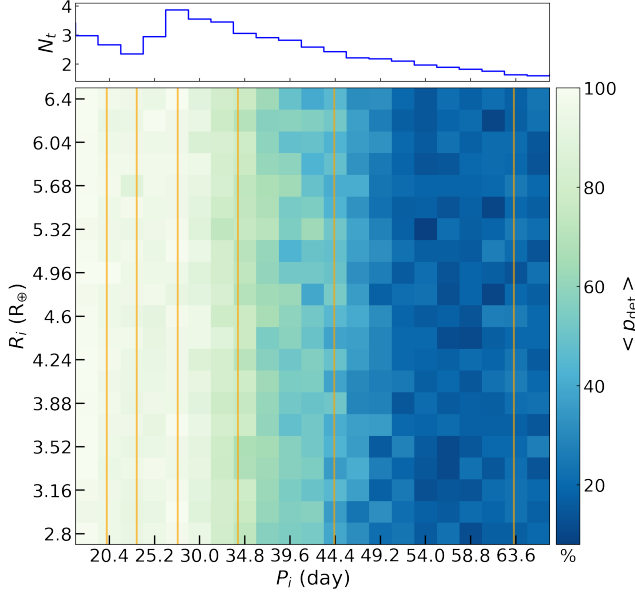


**Figure 12.** The result of the transit injection-and-recovery test for the planet candidate. Blue to light green represents an increasing detection possibility of its transit signal (assuming it transits). The solid blue histogram in the top panel illustrates the average number of transits within the *TESS* time baseline. The foreground yellow solid lines mark the six possible orbital solutions of the planet candidate found in *Juliet*.

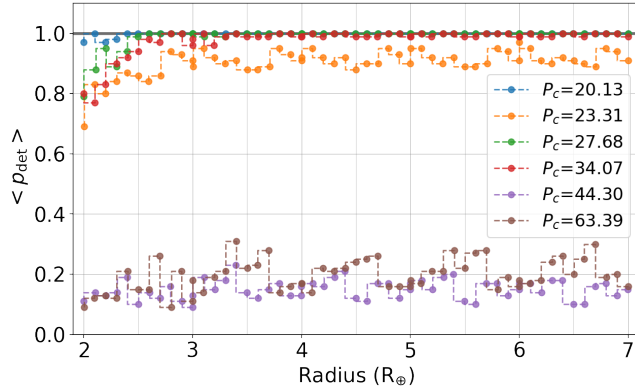


**Figure 13.** Detection probability as a function of the planet radius. Different colors correspond to six possible periods of the planet candidate estimated from *Juliet*, as shown in the legend. The results here incorporate the phase information from the RV data, and thus they are different from Figure 12, which used random phase.

system in a stable configuration if the inner planet loses less than 5-10% of its total mass in a timescale larger than  $2 \times 10^4$  years (Matsumoto & Ogiwara 2020; Wang & Lin 2023). After such “gentle” mass loss process, a closely packed system could still remain stable. On the other hand, if the inner super-Earth experiences a vi-

olent atmosphere mass loss in a shorter timescale, in which about 20-30% of its total mass is lost, a widely separated configuration may form as a consequence of violent dynamical interactions, including collisions and merges between planets. Therefore, the well-separated configuration of TOI-784 system is consistent with the possibility that the inner planet once held a considerably amount of atmosphere.

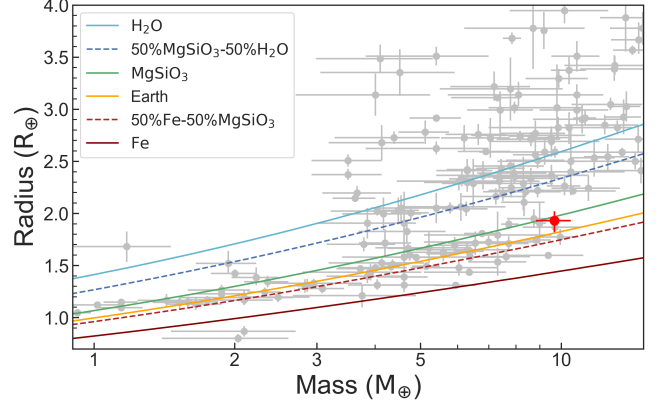


**Figure 14.** The M-R relation. The background gray dots are planets from TEPCAT database. Solid and dashed curves indicate different planet compositions. TOI-784b (the red point) is between the green and orange lines representing a  $\text{MgSiO}_3$  core and Earth composition respectively, which implies that TOI-784b is a rocky planet, the same as our analyses. Considering the uncertainty of the planet size, TOI-784b could be pure rocky or have a small amount of atmospheres consisting of heavy elements (e.g.  $\text{H}_2\text{O}$ ,  $\text{CO}_2$ , etc.).

In addition to the mass loss formation scenario for TOI-784b, there is another possibility that this rocky planet could be a failed core and preserved as a super-Earth in the natal disk (e.g., Ida & Lin 2004). According to Chen et al. (2020), even though a massive core reaches the pebble-isolation mass (few to  $10 M_{\oplus}$ ) before the severe depletion of the gas disk (which is different from formation in a gas-poor environment), an increasing grain opacity in the planetary envelope could significantly suppress the runaway gas accretion given its stellar proximity.

In summary, we confirmed a *TESS* discovered transiting super-Earth, TOI-784b, and identified an additional planet candidate in the system using radial velocities taken by Magellan/PFS, CHIRON, and LCOGT/NRES. TOI-784b is a  $1.93 R_{\oplus}$  super-Earth, with a period of 2.80 days and mass of  $9.67 M_{\oplus}$ . The bulk density of TOI-784b indicates that its composition is likely rocky, with a minimum amount of volatiles, which is consistent with the prediction of the photoe-

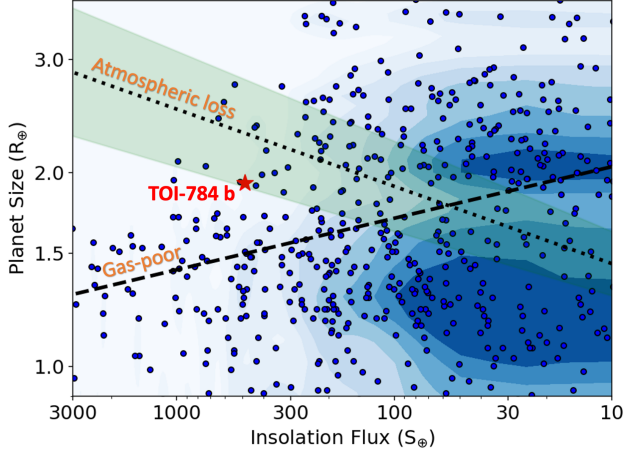


**Figure 15.** Relation of planet insolation flux and radius. Forward blue points are exoplanets with data taken from the NASA exoplanet archive and background contours indicate their number density. The dashed line illustrates theoretical predictions under gas-poor formation scenarios (Lopez & Rice 2018), while the black dotted line is derived by (Martinez et al. 2019) using the CKS sample with the shaded green region representing the  $1\sigma$  error.

vaporization or core-powered mass loss scenario. We also found a planet candidate revealed by the RV follow-up observations, but unfortunately, our observed RVs did not map out its entire orbit. We performed a grid search in parameter space using *RadVel* as well as a two-planet fit using *Juliet* to investigate possible solutions for the planet candidate (Section 4.2). Six possible orbital solutions for the candidate have been found, with the period ranging from 20 to 63 days and mass being  $12 - 31 M_{\oplus}$ . Given its large minimum mass, the candidate is likely a Neptune-mass planet rich in volatiles, unlike TOI-784b. We performed an injection-recovery test to characterize the likelihood of the planet candidate actually transiting but being missed by *TESS*, and we conclude that it is more likely to be an intrinsically non-transiting planet, although we cannot rule out the transit scenario completely, especially if it has a period around or longer than 40 days.

The TOI-784 system contains a transiting small planet in the inner orbit and an outer, likely warm, planet candidate that probably does not transit, which can contribute to the statistical sample of multi-planet systems with mass measurements. The determination of the outer planet candidate’s properties requires future observations, especially more *TESS* observations in the Extended Mission and more RV follow-up.

## 6. ACKNOWLEDGMENTS

We thank Richard Grumitt for his insightful advice on MCMC and Nested Sampling for highly multi-modal

scenarios. We thank David Latham for his helpful suggestions about RV modeling. We thank Marshall Johnson for his contributions to NRES RVs reduction. We thank Xiaochen Zheng for her helpful discussions about the planet formation theory. D. D. acknowledges support from the TESS Guest Investigator Program grants 80NSSC21K0108 and 80NSSC22K0185. Hua and Wang acknowledge support from NSFC grant 12273016. We acknowledge the use of public TESS data from pipelines at the TESS Science Office and at the TESS Science Processing Operations Center. Resources supporting this work were provided by the NASA High-End Computing (HEC) Program through the NASA Advanced Supercomputing (NAS) Division at Ames Research Center for the production of the SPOC data products. This paper includes data collected with the TESS mission, obtained from the MAST data archive at the Space Telescope Science Institute (STScI). Funding for the TESS mission is provided by the NASA Explorer Program. STScI is operated by the Association of Universities for Research in Astronomy, Inc., under NASA contract NAS 5–26555. All the *TESS* data used in this paper can be found in MAST: <https://doi.org/10.17909/fwdt-2x66>. This research has made use of the Exoplanet Follow-up Observation Program website, which is operated by the California Institute of Technology, under contract with the National Aeronautics and Space Administration under the Exoplanet Exploration Program (doi: 10.26134/ExoFOP3). This research has made use of the NASA Exoplanet Archive, which is operated by the California Institute of Technology, under contract with the National Aeronautics and Space Administration under the Exoplanet Exploration Program. This research uses data obtained through the Telescope Access Program (TAP), which has been funded by the TAP member institutes. This work makes use of observations from the Las Cumbres Observatory global telescope network. We acknowledge LCO Key Project (KEY2020B-005) which has kindly offered observing time for the target. This research has used data from the CTIO/SMARTS 1.5m telescope, which is operated as part of the SMARTS Consortium by RECONS ([www.recons.org](http://www.recons.org)) members Todd Henry, Hodari James, Wei-Chun Jao, and Leonardo Paredes. At the telescope, observations were carried out by Roberto Aviles and Rodrigo Hinojosa.

*Facilities:* *TESS*, Magellan(6.5m)-PFS, LCOGT(1m)-NRES, CTIO(1.5m)-CHIRON

*Software:* *astropy* (Astropy Collaboration et al. 2013, 2018, 2022), *emcee* (Foreman-Mackey et al. 2013),

AstroImageJ (Collins et al. 2017), lightkurve (Lightkurve Collaboration et al. 2018), RadVel (Fulton et al. 2018), Juliet (Espinoza et al. 2019), MRExo (Corrales 2015)

Dataset: All the *TESS* light curves used in this paper can be found in MAST: [10.17909/2rfj-4m38](https://mast.stsci.edu/portal/#doc/rep/10.17909/2rfj-4m38). All data we used from ExoFop can be found in [10.26134/Exo-FOP3](https://mast.stsci.edu/portal/#doc/rep/10.26134/Exo-FOP3). All data we used from NASA Exoplanet Archive can be found in [10.26133/NEA13](https://mast.stsci.edu/portal/#doc/rep/10.26133/NEA13).

## REFERENCES

- Astropy Collaboration, Robitaille, T. P., Tollerud, E. J., et al. 2013, *A&A*, 558, A33, doi: [10.1051/0004-6361/201322068](https://doi.org/10.1051/0004-6361/201322068)
- Astropy Collaboration, Price-Whelan, A. M., Sipőcz, B. M., et al. 2018, *AJ*, 156, 123, doi: [10.3847/1538-3881/aabc4f](https://doi.org/10.3847/1538-3881/aabc4f)
- Astropy Collaboration, Price-Whelan, A. M., Lim, P. L., et al. 2022, *ApJ*, 935, 167, doi: [10.3847/1538-4357/ac7c74](https://doi.org/10.3847/1538-4357/ac7c74)
- Ballard, S., & Johnson, J. A. 2016, *ApJ*, 816, 66, doi: [10.3847/0004-637X/816/2/66](https://doi.org/10.3847/0004-637X/816/2/66)
- Barragán, O., Gandolfi, D., Dai, F., et al. 2018, *A&A*, 612, A95, doi: [10.1051/0004-6361/201732217](https://doi.org/10.1051/0004-6361/201732217)
- Batalha, N. E., Lewis, T., Fortney, J. J., et al. 2019, *ApJL*, 885, L25, doi: [10.3847/2041-8213/ab4909](https://doi.org/10.3847/2041-8213/ab4909)
- Batalha, N. M., Rowe, J. F., Bryson, S. T., et al. 2013, *ApJS*, 204, 24, doi: [10.1088/0067-0049/204/2/24](https://doi.org/10.1088/0067-0049/204/2/24)
- Behrard, A., Dai, F., & Howard, A. W. 2022, *AJ*, 163, 160, doi: [10.3847/1538-3881/ac53a7](https://doi.org/10.3847/1538-3881/ac53a7)
- Borucki, W. J., Koch, D., Basri, G., et al. 2010, *Science*, 327, 977, doi: [10.1126/science.1185402](https://doi.org/10.1126/science.1185402)
- Brahm, R., Jordán, A., & Espinoza, N. 2017, *PASP*, 129, 034002, doi: [10.1088/1538-3873/aa5455](https://doi.org/10.1088/1538-3873/aa5455)
- Brandt, T. D. 2021, *The Astrophysical Journal Supplement Series*, 254, 42, doi: [10.3847/1538-4365/abf93c](https://doi.org/10.3847/1538-4365/abf93c)
- Brown, T. M., Baliber, N., Bianco, F. B., et al. 2013, *PASP*, 125, 1031, doi: [10.1086/673168](https://doi.org/10.1086/673168)
- Buchhave, L. A., Latham, D. W., Johansen, A., et al. 2012, *Nature*, 486, 375, doi: [10.1038/nature11121](https://doi.org/10.1038/nature11121)
- Buchner, J., Georgakakis, A., Nandra, K., et al. 2014, *A&A*, 564, A125, doi: [10.1051/0004-6361/201322971](https://doi.org/10.1051/0004-6361/201322971)
- Burt, J., Holden, B., Wolfgang, A., & Bouma, L. G. 2018, *AJ*, 156, 255, doi: [10.3847/1538-3881/aae697](https://doi.org/10.3847/1538-3881/aae697)
- Butler, R. P., Marcy, G. W., Williams, E., et al. 1996, *PASP*, 108, 500, doi: [10.1086/133755](https://doi.org/10.1086/133755)
- Castelli, F., & Kurucz, R. L. 2003, in *Modelling of Stellar Atmospheres*, ed. N. Piskunov, W. W. Weiss, & D. F. Gray, Vol. 210, A20. <https://arxiv.org/abs/astro-ph/0405087>
- Chen, Y.-X., Li, Y.-P., Li, H., & Lin, D. N. C. 2020, *ApJ*, 896, 135, doi: [10.3847/1538-4357/ab9604](https://doi.org/10.3847/1538-4357/ab9604)
- Cloutier, R., & Menou, K. 2020, *AJ*, 159, 211, doi: [10.3847/1538-3881/ab8237](https://doi.org/10.3847/1538-3881/ab8237)
- Cloutier, R., Rodriguez, J. E., Irwin, J., et al. 2020, *AJ*, 160, 22, doi: [10.3847/1538-3881/ab9534](https://doi.org/10.3847/1538-3881/ab9534)
- Collins, K. A., Kielkopf, J. F., Stassun, K. G., & Hessman, F. V. 2017, *AJ*, 153, 77, doi: [10.3847/1538-3881/153/2/77](https://doi.org/10.3847/1538-3881/153/2/77)
- Corrales, L. 2015, *dust: Calculate the intensity of dust scattering halos in the X-ray, 1.0*, Zenodo, doi: [10.5281/zenodo.15991](https://doi.org/10.5281/zenodo.15991)
- Crane, J. D., Shectman, S. A., & Butler, R. P. 2006, in *Proc. SPIE, Vol. 6269, Society of Photo-Optical Instrumentation Engineers (SPIE) Conference Series*, 626931, doi: [10.1117/12.672339](https://doi.org/10.1117/12.672339)
- Crane, J. D., Shectman, S. A., Butler, R. P., et al. 2010, in *Proc. SPIE, Vol. 7735, Ground-based and Airborne Instrumentation for Astronomy III*, 773553, doi: [10.1117/12.857792](https://doi.org/10.1117/12.857792)
- Crane, J. D., Shectman, S. A., Butler, R. P., Thompson, I. B., & Burley, G. S. 2008, in *Proc. SPIE, Vol. 7014, Ground-based and Airborne Instrumentation for Astronomy II*, 701479, doi: [10.1117/12.789637](https://doi.org/10.1117/12.789637)
- Crepp, J. R., Johnson, J. A., Howard, A. W., et al. 2012, *ApJ*, 761, 39, doi: [10.1088/0004-637X/761/1/39](https://doi.org/10.1088/0004-637X/761/1/39)
- Espinoza, N. 2018, *Research Notes of the American Astronomical Society*, 2, 209, doi: [10.3847/2515-5172/aaef38](https://doi.org/10.3847/2515-5172/aaef38)
- Espinoza, N., Kossakowski, D., & Brahm, R. 2019, *MNRAS*, 490, 2262, doi: [10.1093/mnras/stz2688](https://doi.org/10.1093/mnras/stz2688)
- Feroz, F., & Hobson, M. P. 2008, *Monthly Notices of the Royal Astronomical Society*, 384, 449, doi: [10.1111/j.1365-2966.2007.12353.x](https://doi.org/10.1111/j.1365-2966.2007.12353.x)
- Feroz, F., Hobson, M. P., & Bridges, M. 2009, *MNRAS*, 398, 1601, doi: [10.1111/j.1365-2966.2009.14548.x](https://doi.org/10.1111/j.1365-2966.2009.14548.x)
- Feroz, F., Hobson, M. P., Cameron, E., & Pettitt, A. N. 2019, *The Open Journal of Astrophysics*, 2, 1, doi: [10.21105/astro.1306.2144](https://doi.org/10.21105/astro.1306.2144)
- Foreman-Mackey, D., Agol, E., Ambikasaran, S., & Angus, R. 2017, *AJ*, 154, 220, doi: [10.3847/1538-3881/aa9332](https://doi.org/10.3847/1538-3881/aa9332)
- Foreman-Mackey, D., Hogg, D. W., Lang, D., & Goodman, J. 2013, *PASP*, 125, 306, doi: [10.1086/670067](https://doi.org/10.1086/670067)
- Fulton, B. J., & Petigura, E. A. 2018, *AJ*, 156, 264, doi: [10.3847/1538-3881/aae828](https://doi.org/10.3847/1538-3881/aae828)
- Fulton, B. J., Petigura, E. A., Blunt, S., & Sinukoff, E. 2018, *PASP*, 130, 044504, doi: [10.1088/1538-3873/aaaaa8](https://doi.org/10.1088/1538-3873/aaaaa8)

- Fulton, B. J., Petigura, E. A., Howard, A. W., et al. 2017, *AJ*, 154, 109, doi: [10.3847/1538-3881/aa80eb](https://doi.org/10.3847/1538-3881/aa80eb)
- Gaia Collaboration. 2018, *VizieR Online Data Catalog*, I/345
- . 2020, *VizieR Online Data Catalog*, I/350
- Gan, T., Wang, S. X., Wang, S., et al. 2022, arXiv e-prints, arXiv:2210.08313. <https://arxiv.org/abs/2210.08313>
- Ginzburg, S., Schlichting, H. E., & Sari, R. 2018, *MNRAS*, 476, 759, doi: [10.1093/mnras/sty290](https://doi.org/10.1093/mnras/sty290)
- Guerrero, N. M., Seager, S., Huang, C. X., et al. 2021, *ApJS*, 254, 39, doi: [10.3847/1538-4365/abefel](https://doi.org/10.3847/1538-4365/abefel)
- Gupta, A., & Schlichting, H. E. 2020, *MNRAS*, 493, 792, doi: [10.1093/mnras/staa315](https://doi.org/10.1093/mnras/staa315)
- Hamilton, D. P., & Burns, J. A. 1992, *Icarus*, 96, 43, doi: [https://doi.org/10.1016/0019-1035\(92\)90005-R](https://doi.org/10.1016/0019-1035(92)90005-R)
- Hansen, B. M. S., & Murray, N. 2013, *ApJ*, 775, 53, doi: [10.1088/0004-637X/775/1/53](https://doi.org/10.1088/0004-637X/775/1/53)
- Haywood, R. D., Collier Cameron, A., Queloz, D., et al. 2014, *MNRAS*, 443, 2517, doi: [10.1093/mnras/stu1320](https://doi.org/10.1093/mnras/stu1320)
- He, M. Y., Ford, E. B., & Ragozzine, D. 2019, *MNRAS*, 490, 4575, doi: [10.1093/mnras/stz2869](https://doi.org/10.1093/mnras/stz2869)
- He, M. Y., Ford, E. B., Ragozzine, D., & Carrera, D. 2020, *The Astronomical Journal*, 160, 276, doi: [10.3847/1538-3881/abba18](https://doi.org/10.3847/1538-3881/abba18)
- Henry, T. J., Soderblom, D. R., Donahue, R. A., & Baliunas, S. L. 1996, *The Astrophysical Journal*, 111, 439
- Howell, S. B., Everett, M. E., Sherry, W., Horch, E., & Ciardi, D. R. 2011, *Astronomical Journal*, 142, doi: [10.1088/0004-6256/142/1/19](https://doi.org/10.1088/0004-6256/142/1/19)
- Ida, S., & Lin, D. N. C. 2004, *ApJ*, 604, 388, doi: [10.1086/381724](https://doi.org/10.1086/381724)
- Jenkins, J. M. 2002, *ApJ*, 575, 493, doi: [10.1086/341136](https://doi.org/10.1086/341136)
- Jenkins, J. M., Tenenbaum, P., Seader, S., et al. 2020, *Kepler Data Processing Handbook: Transiting Planet Search*, Kepler Science Document KSCI-19081-003, id. 9. Edited by Jon M. Jenkins.
- Jenkins, J. M., Chandrasekaran, H., McCauliff, S. D., et al. 2010, *Software and Cyberinfrastructure for Astronomy*, 7740, 77400D, doi: [10.1117/12.856764](https://doi.org/10.1117/12.856764)
- Jenkins, J. M., Twicken, J. D., McCauliff, S., et al. 2016, in *Society of Photo-Optical Instrumentation Engineers (SPIE) Conference Series*, Vol. 9913, Proc. SPIE, 99133E, doi: [10.1117/12.2233418](https://doi.org/10.1117/12.2233418)
- Jensen, E. 2013, *Tapir: A web interface for transit/eclipse observability*. <http://ascl.net/1306.007>
- Kempton, E. M., Bean, J. L., Louie, D. R., et al. 2018, *Publications of the Astronomical Society of the Pacific*, 130, 1, doi: [10.1088/1538-3873/aadf6f](https://doi.org/10.1088/1538-3873/aadf6f)
- Kovács, G., Zucker, S., & Mazeh, T. 2002, *A&A*, 391, 369. <https://www.aanda.org/articles/aa/pdf/2002/31/aa2422.pdf>
- Kreidberg, L. 2015, *PASP*, 127, 1161, doi: [10.1086/683602](https://doi.org/10.1086/683602)
- Kurucz, R. L. 1979, *ApJS*, 40, 1, doi: [10.1086/190589](https://doi.org/10.1086/190589)
- Lacedelli, G., Malavolta, L., Borsato, L., et al. 2021, *MNRAS*, 501, 4148, doi: [10.1093/mnras/staa3728](https://doi.org/10.1093/mnras/staa3728)
- Lehtinen, J., Jetsu, L., Hackman, T., Kajatkari, P., & Henry, G. W. 2016, *Astronomy and Astrophysics*, 588, 1, doi: [10.1051/0004-6361/201527420](https://doi.org/10.1051/0004-6361/201527420)
- Li, J., Tenenbaum, P., Twicken, J. D., et al. 2019, *PASP*, 131, 024506, doi: [10.1088/1538-3873/aaf44d](https://doi.org/10.1088/1538-3873/aaf44d)
- Lightkurve Collaboration, Cardoso, J. V. d. M., Hedges, C., et al. 2018, *Lightkurve: Kepler and TESS time series analysis in Python*, *Astrophysics Source Code Library*. <http://ascl.net/1812.013>
- Lissauer, J. J., Ragozzine, D., Fabrycky, D. C., et al. 2011, *Astrophysical Journal*, Supplement Series, 197, doi: [10.1088/0067-0049/197/1/8](https://doi.org/10.1088/0067-0049/197/1/8)
- Lopez, E. D., & Rice, K. 2018, *MNRAS*, 479, 5303, doi: [10.1093/mnras/sty1707](https://doi.org/10.1093/mnras/sty1707)
- Lubin, J., Van Zandt, J., Holcomb, R., et al. 2022, *AJ*, 163, 101, doi: [10.3847/1538-3881/ac3d38](https://doi.org/10.3847/1538-3881/ac3d38)
- Luque, R., & Pallé, E. 2022, *Science*, 377, 1211, doi: [10.1126/science.abl7164](https://doi.org/10.1126/science.abl7164)
- Mamajek, E. E., & Hillenbrand, L. A. 2008, *ApJ*, 687, 1264, doi: [10.1086/591785](https://doi.org/10.1086/591785)
- Martinez, C. F., Cunha, K., Ghezzi, L., & Smith, V. V. 2019, *ApJ*, 875, 29, doi: [10.3847/1538-4357/ab0d93](https://doi.org/10.3847/1538-4357/ab0d93)
- Matsumoto, Y., & Ogihara, M. 2020, *The Astrophysical Journal*, 893, 43, doi: [10.3847/1538-4357/ab7cd7](https://doi.org/10.3847/1538-4357/ab7cd7)
- Mermilliod, J. C. 2006, *VizieR Online Data Catalog*, II/168
- Montet, B. T., Crepp, J. R., Johnson, J. A., Howard, A. W., & Marcy, G. W. 2014, *ApJ*, 781, 28, doi: [10.1088/0004-637X/781/1/28](https://doi.org/10.1088/0004-637X/781/1/28)
- Mulders, G. D., Pascucci, I., Apai, D., & Ciesla, F. J. 2018, *The Astronomical Journal*, 156, 24, doi: [10.3847/1538-3881/aac5ea](https://doi.org/10.3847/1538-3881/aac5ea)
- Owen, J. E., & Wu, Y. 2017, *ArXiv e-prints*. <https://arxiv.org/abs/1705.10810>
- Paredes, L. A., Henry, T. J., Quinn, S. N., et al. 2021, *The Astronomical Journal*, 162, 176, doi: [10.3847/1538-3881/ac082a](https://doi.org/10.3847/1538-3881/ac082a)
- Petigura, E. A., Rogers, J. G., Isaacson, H., et al. 2022, *The Astronomical Journal*, 163, 179, doi: [10.3847/1538-3881/ac51e3](https://doi.org/10.3847/1538-3881/ac51e3)
- Ricker, G. R., Winn, J. N., Vanderpek, R., et al. 2015, *Journal of Astronomical Telescopes, Instruments, and Systems*, 1, 014003, doi: [10.1117/1.JATIS.1.1.014003](https://doi.org/10.1117/1.JATIS.1.1.014003)

- Salomone, R., South, L. F., Drovandi, C. C., & Kroese, D. P. 2018, arXiv e-prints, arXiv:1805.03924, doi: [10.48550/arXiv.1805.03924](https://doi.org/10.48550/arXiv.1805.03924)
- Schlegel, D. J., Finkbeiner, D. P., & Davis, M. 1998, ApJ, 500, 525, doi: [10.1086/305772](https://doi.org/10.1086/305772)
- Seager, S., & Mallén-Ornelas, G. 2003, ApJ, 585, 1038, doi: [10.1086/346105](https://doi.org/10.1086/346105)
- Siverd, R. J., Brown, T. M., Barnes, S., et al. 2018, in Society of Photo-Optical Instrumentation Engineers (SPIE) Conference Series, Vol. 10702, Ground-based and Airborne Instrumentation for Astronomy VII, ed. C. J. Evans, L. Simard, & H. Takami, 107026C, doi: [10.1117/12.2312800](https://doi.org/10.1117/12.2312800)
- Smith, J. C., Stumpe, M. C., Van Cleve, J. E., et al. 2012, PASP, 124, 1000, doi: [10.1086/667697](https://doi.org/10.1086/667697)
- Southworth, J. 2011, Monthly Notices of the Royal Astronomical Society, 417, 2166, doi: [10.1111/j.1365-2966.2011.19399.x](https://doi.org/10.1111/j.1365-2966.2011.19399.x)
- Speagle, J. S. 2019, arXiv e-prints, arXiv:1904.02180. <https://arxiv.org/abs/1904.02180>
- Stassun, K. G., Collins, K. A., & Gaudi, B. S. 2017, AJ, 153, 136, doi: [10.3847/1538-3881/aa5df3](https://doi.org/10.3847/1538-3881/aa5df3)
- Stassun, K. G., & Torres, G. 2016, AJ, 152, 180, doi: [10.3847/0004-6256/152/6/180](https://doi.org/10.3847/0004-6256/152/6/180)
- . 2018, ApJ, 862, 61, doi: [10.3847/1538-4357/aacafc](https://doi.org/10.3847/1538-4357/aacafc)
- . 2021, ApJL, 907, L33, doi: [10.3847/2041-8213/abdaad](https://doi.org/10.3847/2041-8213/abdaad)
- Stumpe, M. C., Smith, J. C., Catanzarite, J. H., et al. 2014, PASP, 126, 100, doi: [10.1086/674989](https://doi.org/10.1086/674989)
- Stumpe, M. C., Smith, J. C., Van Cleve, J. E., et al. 2012, PASP, 124, 985, doi: [10.1086/667698](https://doi.org/10.1086/667698)
- Tayar, J., Claytor, Z. R., Huber, D., & van Saders, J. 2022, ApJ, 927, 31, doi: [10.3847/1538-4357/ac4bbc](https://doi.org/10.3847/1538-4357/ac4bbc)
- Teske, J., Wang, S. X., Wolfgang, A., et al. 2021, ApJS, 256, 33, doi: [10.3847/1538-4365/ac0f0a](https://doi.org/10.3847/1538-4365/ac0f0a)
- Tokovinin, A. 2018, PASP, 130, 035002, doi: [10.1088/1538-3873/aaa7d9](https://doi.org/10.1088/1538-3873/aaa7d9)
- Tokovinin, A., Fischer, D. A., Bonati, M., et al. 2013, Publications of the Astronomical Society of the Pacific, 125, 1336, doi: [10.1086/674012](https://doi.org/10.1086/674012)
- Torres, G., Andersen, J., & Giménez, A. 2010, A&A Rv, 18, 67, doi: [10.1007/s00159-009-0025-1](https://doi.org/10.1007/s00159-009-0025-1)
- Trotta, R. 2008, Contemporary Physics, 49, 71, doi: [10.1080/00107510802066753](https://doi.org/10.1080/00107510802066753)
- Twicken, J. D., Catanzarite, J. H., Clarke, B. D., et al. 2018, PASP, 130, 064502, doi: [10.1088/1538-3873/aab694](https://doi.org/10.1088/1538-3873/aab694)
- Wang, S., & Lin, D. N. C. 2023, AJ, 165, 174, doi: [10.3847/1538-3881/acc070](https://doi.org/10.3847/1538-3881/acc070)
- Weiss, L. M., Millholland, S. C., Petigura, E. A., et al. 2022, arXiv e-prints, arXiv:2203.10076, doi: [10.48550/arXiv.2203.10076](https://doi.org/10.48550/arXiv.2203.10076)
- Weiss, L. M., Isaacson, H. T., Marcy, G. W., et al. 2018, The Astronomical Journal, 156, 254, doi: [10.3847/1538-3881/aae70a](https://doi.org/10.3847/1538-3881/aae70a)
- Wolfgang, A., Rogers, L. A., & Ford, E. B. 2016, ApJ, 825, 19, doi: [10.3847/0004-637X/825/1/19](https://doi.org/10.3847/0004-637X/825/1/19)
- Zechmeister, M., & Kürster, M. 2009, A&A, 496, 577, doi: [10.1051/0004-6361:200811296](https://doi.org/10.1051/0004-6361:200811296)
- Zeng, L., Sasselov, D. D., & Jacobsen, S. B. 2016, ApJ, 819, 127, doi: [10.3847/0004-637X/819/2/127](https://doi.org/10.3847/0004-637X/819/2/127)
- Zhou, G., Quinn, S. N., Irwin, J., et al. 2020, The Astronomical Journal, 161, 2, doi: [10.3847/1538-3881/abba22](https://doi.org/10.3847/1538-3881/abba22)
- Zhu, W., Petrovich, C., Wu, Y., Dong, S., & Xie, J. 2018, ApJ, 860, 101, doi: [10.3847/1538-4357/aac6d5](https://doi.org/10.3847/1538-4357/aac6d5)
- Ziegler, C., Tokovinin, A., Briceño, C., et al. 2020, AJ, 159, 19, doi: [10.3847/1538-3881/ab55e9](https://doi.org/10.3847/1538-3881/ab55e9)
- Zink, J. K., Christiansen, J. L., & Hansen, B. M. S. 2019, MNRAS, 483, 4479, doi: [10.1093/mnras/sty3463](https://doi.org/10.1093/mnras/sty3463)

## APPENDIX

## A. ONE-PLANET FIT

Due to a lack of RV data, we cannot fully constrain the orbit of the additional planet candidate (which we called “planet c” for simplicity in the paper), planet b’s solution would be dependent on the choice of the specific two-planet fit. In this appendix, we explore the robustness of planet b’s parameters and check if we could constrain the mass of planet b regardless of the choice for the orbital solution of the planet candidate.

Before we obtained the 4 more data points in 2022 from PFS, the PFS data had unfortunately only captured the same rising phase of the second planet separated by a year, which makes it challenging for the RV analysis due to degeneracy in the period and RV amplitude parameter space for the second object. Therefore, we first constructed a composite model with a linear trend for each of the first two sections of PFS data plus a Keplerian model for planet b, which would be a more generic model describing the signals from the second object more commonly used in the RV fit for systems with long-period massive companions (e.g., [Crepp et al. 2012](#); [Montet et al. 2014](#)). Here we present the result of our fit to the pre-2022 PFS RVs using this simple model that consists of one Keplerian model plus two trends. An alternative model including both a linear trend and a curvature has also been tested, but model comparison with BIC and  $AIC_c$  indicates that this was not the favored model.

The best-fit Keplerian + 2 trends model is shown in Figure 16. Similar to Section 4.2.1, we used *RadVel* ([Fulton et al. 2018](#)) to perform this fit, where a maximum a posteriori optimization (MAP) will first be run in a fit via `scipy.optimize.minimize`, followed by a MCMC analysis via *emcee* ([Foreman-Mackey et al. 2013](#)) to estimate the uncertainty for each parameter. In our case, we required the model to fit two independent linear trends, which is not supported by *RadVel*, so we modified its source code and added an additional term in the model.

Priors and best-fit values are listed in table 9. To be specific, we gave normal distributions for the orbital period  $P_b$  and the time-of-transit center  $t_{0,b}$  according to the optimized values we obtained in the previous photometry analysis (Section 4.1). Eccentricity was fixed to zero as we discussed in Section 4.1.1. The initial guess of  $K_b$  was 5 m/s and we set a uniform distribution of  $\mathcal{U}(-20, 20)$  for its prior, which is roughly twice the RV range of PFS data used here. We gave two different slopes  $\dot{\gamma}_1, \dot{\gamma}_2$  for the two sections of RV data with initial guesses both set to zero. The two sections of data share a same jitter term  $\sigma_{\text{PFS}}$  but having independent offset terms  $\mu_{\text{PFS},1}, \mu_{\text{PFS},2}$  of PFS, for which we gave normal distribution  $\mathcal{N}(0, 10^2)$  and two uniform distributions  $\mathcal{U}(0, 15)$ , respectively. The best-fit RV semi-amplitude of planet b  $K_b$  and its uncertainties are  $4.59^{+0.28}_{-0.29}$  m/s, and the corresponding minimum mass is  $9.47^{+0.92}_{-0.90} M_{\oplus}$ , consistent with the values we presented in the main text of this paper (Table 8). Corner plots for the marginalized posteriors of the fitted and the derived parameters are presented in Figure 17 and Figure 18.

We then subtracted the best-fit linear trends from the RV data and performed a joint fit using *Juliet* ([Espinoza et al. 2019](#)) combining the residual RV data with the *TESS* light curve (Figure 19). The joint fit did not tighten the constraints on any of the parameters for planet b, and the results are consistent well within their error bars with our results presented above (Section 4).

We also performed a one-planet fit in *RadVel* including a Gaussian Process (GP) model to fit the additional RV signals besides TOI-784b. A GP model is a commonly used generic non-parametric model describing periodic or quasiperiod signals, more often used to describe RV jitter caused by stellar magnetic activities (e.g., [Haywood et al. 2014](#)). Here we chose to use the GP regression to model the RVs from the planet candidate as it is a flexible and generic time-series model that does not bear any astrophysical meanings, which is ideal to test the robustness of planet b’s orbital solution. We used the quasi-periodic kernel implemented by *celerite* ([Foreman-Mackey et al. 2017](#)) as offered in *RadVel*. The results for our GP + planet b model are shown in Figure 20 and Table 10. The derived  $M_b \sin i_b$  is  $9.49^{+0.97}_{-0.94} M_{\oplus}$ , consistent with our results in Table 8 and also consistent with the results using the model with the two linear trends.

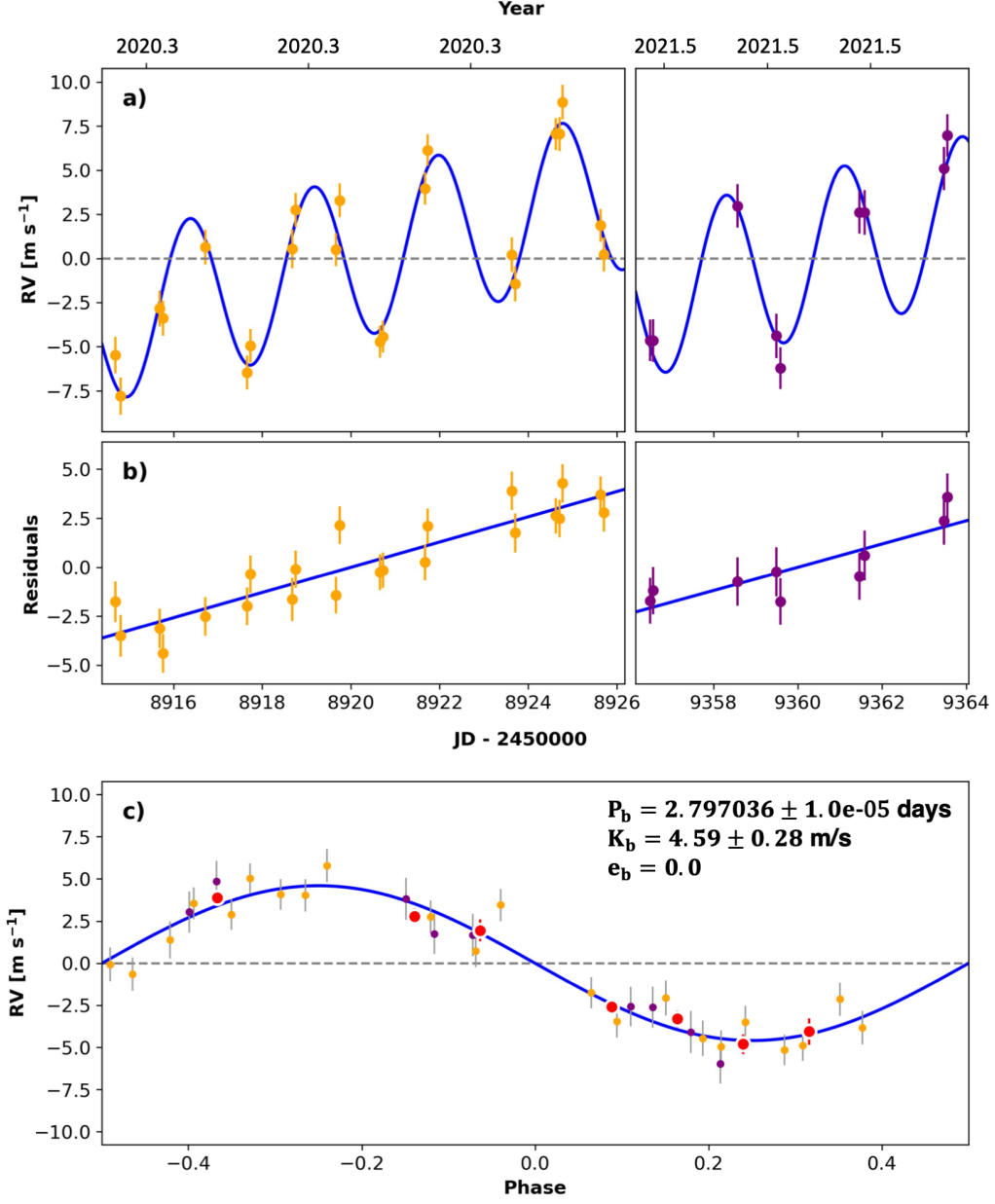


**Figure 16.** The one-planet RV fit with two independent trends in the model. The orange and purple dots represent the first and second year PFS data, respectively. The best-fit model is shown by the thin blue line. (b) The linear residuals after subtracting signals from TOI-784b. (c) The phase-folded RV plot of TOI-784b. Red circles are the same velocities binned in 0.08 units of the orbital phase.

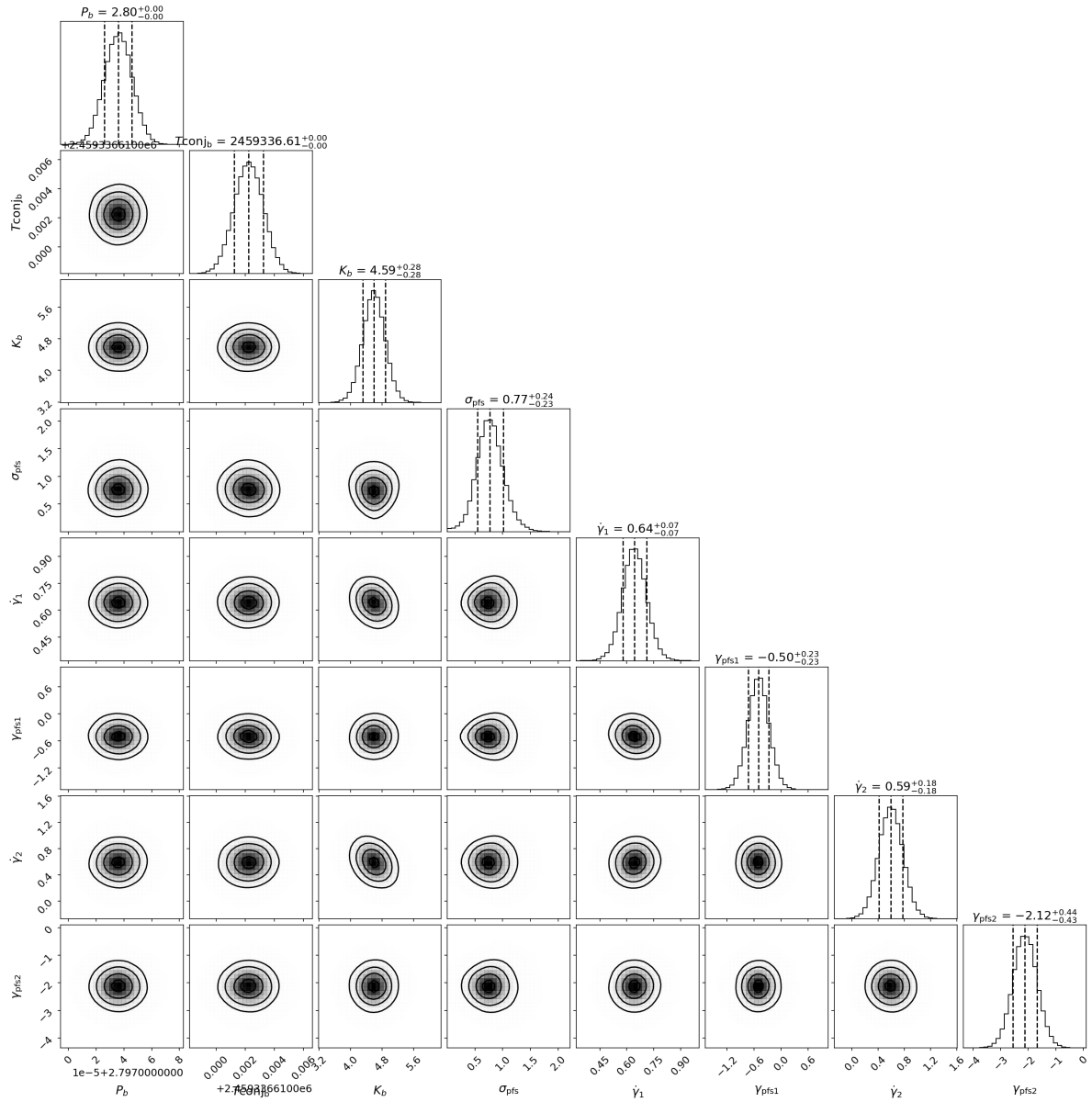


**Figure 17.** Corner plot of all fitted parameters in one-planet RV fit using RadVel.

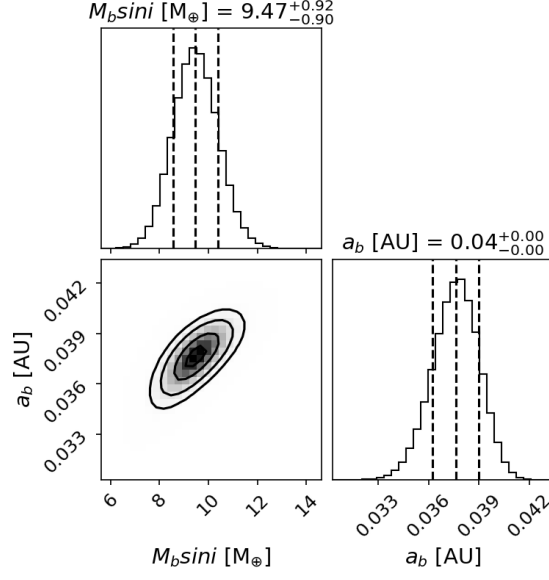


**Figure 18.** Corner plot of derived parameters in one-planet RV fit using RadVel.

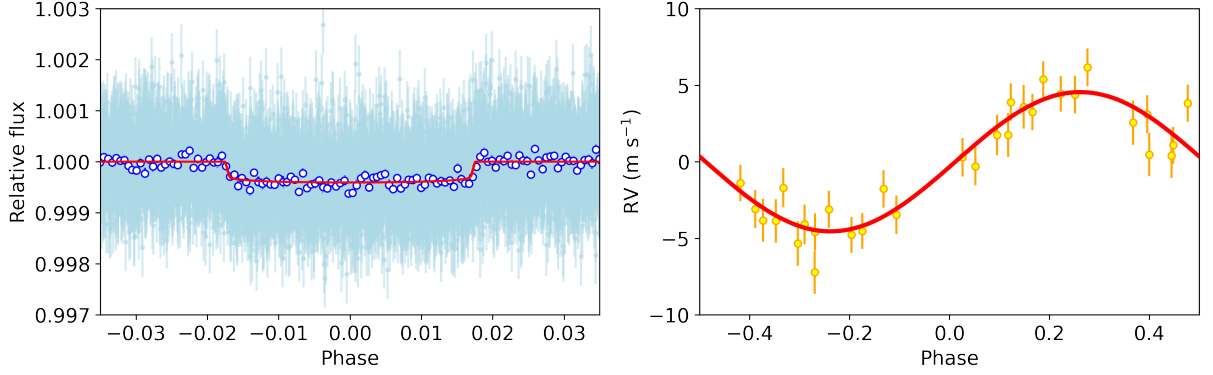


**Figure 19.** The joint fit of the *TESS* light curve and RVs of planet b using pre-2022 PFS RVs with the two best-fit linear trends subtracted. The transit fit is in the left panel, and the RV fit is on the right, with the best-fit model in red solid lines. The white dots circled by blue rings are binned *TESS* photometric data points with a 40 bin size.

**Table 9.** Priors and best-fit values of one-planet fit

Parameter	Prior	Best-fit	Description
$P_b$ (day)	$\mathcal{N}(2.7970364, 0.00001^2)$	$2.797036^{+0.000010}_{-0.000010}$	Orbital period of TOI-784b
$t_{0,b}$ (BJD)	$\mathcal{N}(2459336.61220, 0.001^2)$	$2459336.6122^{+0.0010}_{-0.0010}$	Time of transit-center for TOI-784b
$\sqrt{e_b} \sin \omega_b$	Fixed	0	
$\sqrt{e_b} \cos \omega_b$	Fixed	0	
$K_b$ (m/s)	$\mathcal{U}(-20.0, 20.0)$	$4.59^{+0.28}_{-0.29}$	RV semi-amplitude of TOI-784b
$\dot{\gamma}_1$	RadVel default	$0.643^{+0.067}_{-0.065}$	Linear trend term in the RV fit
$\ddot{\gamma}_1$	Fixed	0	Curvature term in the RV fit
$\dot{\gamma}_2$	RadVel default	$0.59^{+0.18}_{-0.18}$	Linear trend term in the RV fit
$\ddot{\gamma}_2$	Fixed	0	Curvature term in the RV fit
$\mu_{\text{PFS},1}$	$\mathcal{N}(0.0, 10.0^2)$	$0.50^{+0.23}_{-0.23}$	Velocity zero-point for PFS
$\mu_{\text{PFS},2}$	$\mathcal{N}(0.0, 10.0^2)$	$-2.12^{+0.44}_{-0.43}$	Velocity zero-point for PFS
$\sigma_{\text{PFS}}$	$\mathcal{U}(0.0, 15.0)$	$0.77^{+0.24}_{-0.23}$	Jitter term for PFS

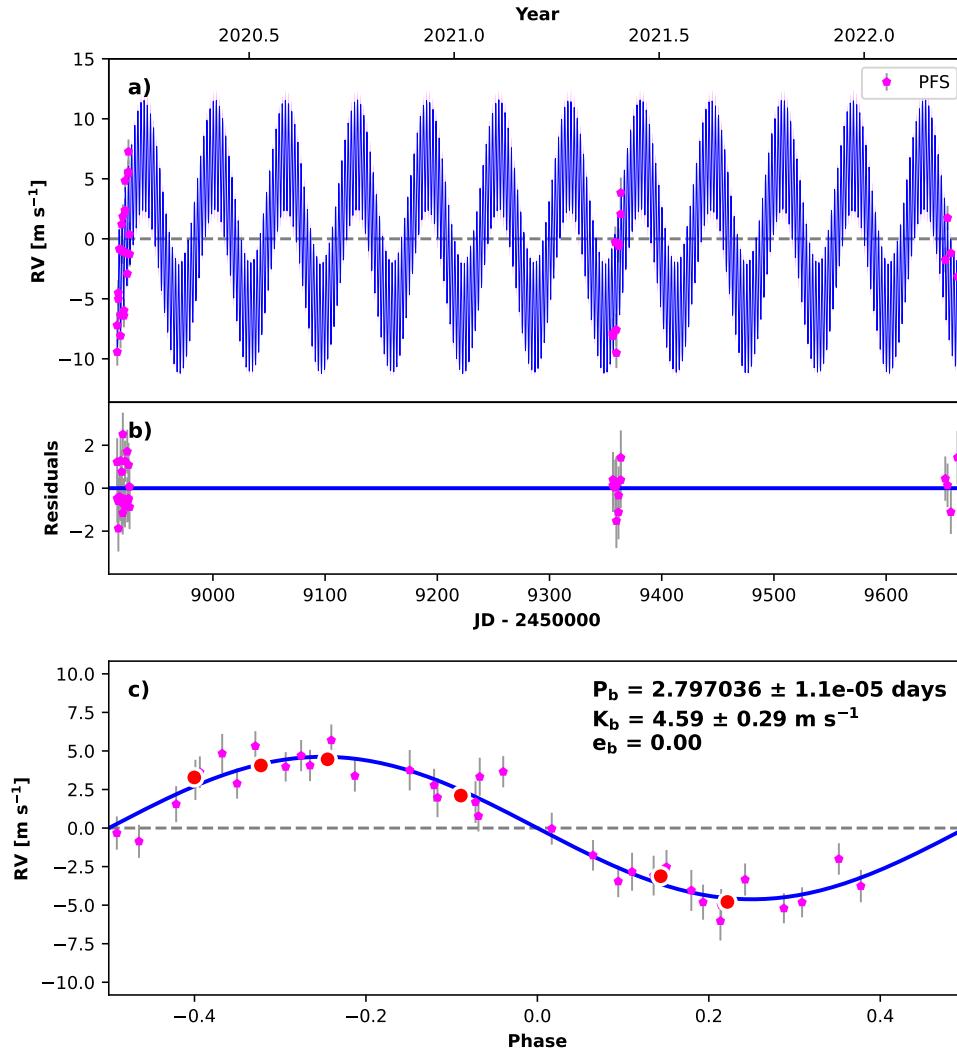


**Figure 20.** The one-planet RV fit with a GP model using `RadVel` and `celerite`. The magenta points are the used PFS RVs. The best-fit model is shown by the thin blue line. (b) The RV residuals after subtracting the best fit GP and Keplerian models. (c) The phase-folded RV plot of TOI-784b after subtracting the GP model component. Red circles are the same velocities binned in 0.08 units of orbital phase.

**Table 10.** Priors and best-fit values of one-planet fit including a GP model

Parameter	Prior	Best-fit	Description
Planetary parameters			
$P_b$ (day)	$\mathcal{N}(2.7970364, 0.00001^2)$	$2.797036^{+1.0e-5}_{-1.1e-5}$	Orbital period of TOI-784b
$t_{0,b}$ (BJD)	$\mathcal{N}(2459336.61220, 0.001^2)$	$2459336.6122^{+0.0011}_{-0.0010}$	Time of transit-center for TOI-784b
$\sqrt{e_b} \sin \omega_b$	Fixed	0	
$\sqrt{e_b} \cos \omega_b$	Fixed	0	
$K_b$ (m/s)	$\mathcal{U}(-20.0, 20.0)$	$4.59^{+0.32}_{-0.30}$	RV semi-amplitude of TOI-784b
$\dot{\gamma}$	Fixed	0	Linear trend term in the RV fit
$\ddot{\gamma}$	Fixed	0	Curvature term in the RV fit
$\mu_{\text{PFS}}$	$\mathcal{N}(0.0, 10.0^2)$	$-0.30^{+6.0}_{-4.8}$	Velocity zero-point for PFS
$\sigma_{\text{PFS}}$	$\mathcal{U}(0.0, 15.0)$	$0.82^{+0.25}_{-0.22}$	Jitter term for PFS
Gaussian process parameters			
$B_{\text{PFS}}$	$\mathcal{U}(0.0001, 10000)$	$76^{+680}_{-61}$	GP hyperparameter
$C_{\text{PFS}}$	$\mathcal{U}(0.0001, 10000)$	$0.006^{+0.23}_{-0.0057}$	GP hyperparameter
$L_{\text{PFS}}$	$\mathcal{U}(0.0001, 1.0e + 7)$	$6254^{+2600}_{-3300}$	GP hyperparameter
$P_{\text{rot,PFS}}$	$\mathcal{U}(10.0, 450.0)$	$54^{+160}_{-27}$	GP hyperparameter

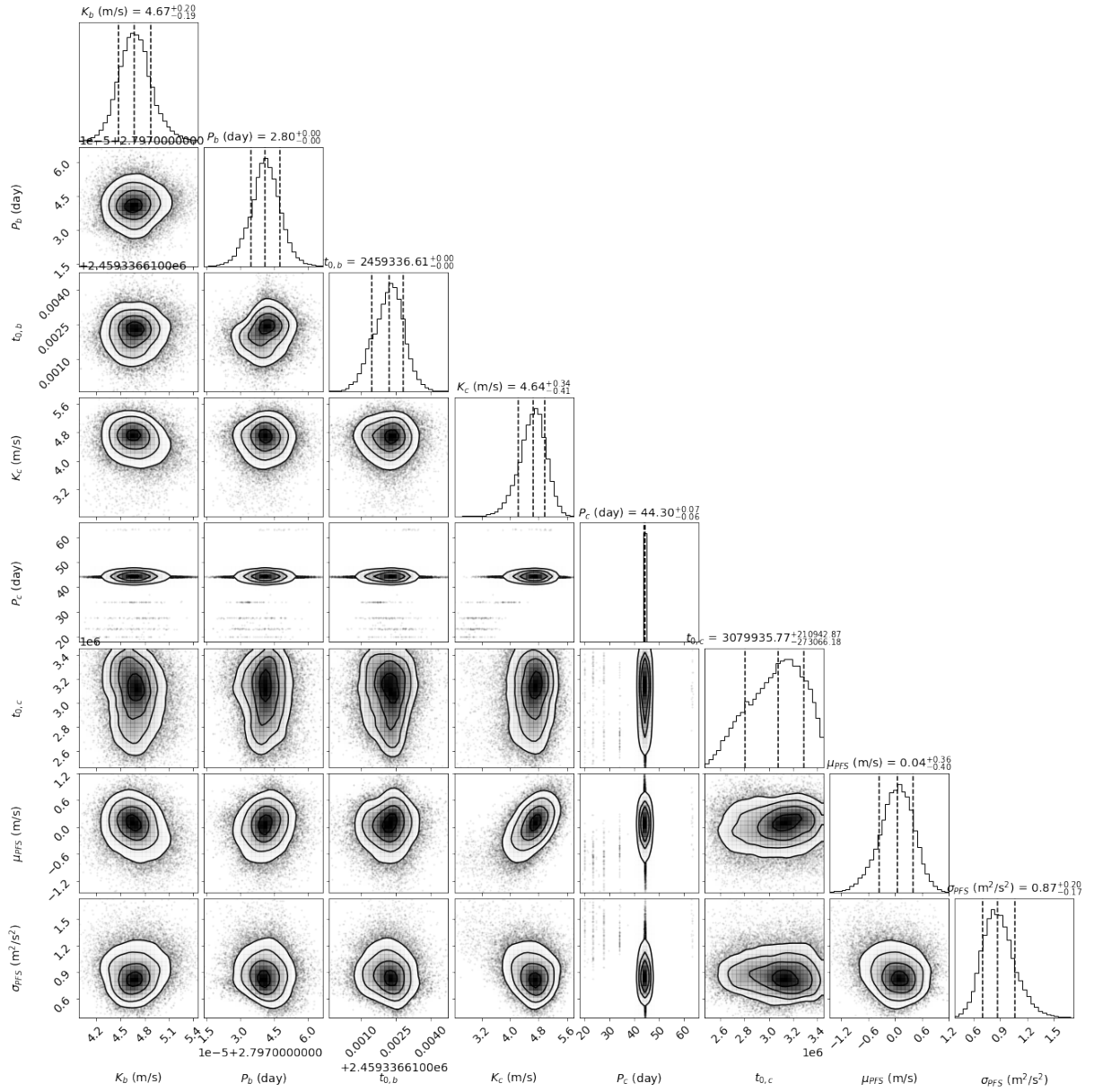


**Figure 21.** Corner plot of all fitted parameters in the two-planet fit using Juliet. See Section 4.2.2 for more details.